Chapter 1
Multilayer Mirrors for Attosecond Pulses

Alexander Guggenmos and Ulf Kleineberg

1.1. Introduction

Multilayer-based optics have been developed into well-established optical components for steering [1], focusing [2], polarizing [3] and spectral filtering [4] of soft x-ray radiation since its first description by Spiller in 1976 [5].

Their significant advantage compared to single-surface grazing incidence optics working in external total reflection lays in an increased glancing angle, even up to near-normal incidence, larger collection angles, better imaging performance due to decreased astigmatism, and tailor-made spectral filtering. However, in many cases multilayer reflectors do not reach the high reflectance values of grazing incidence mirrors and are limited to peak reflectances slightly above 70 % at best, mainly due to absorption and scattering losses [6].

Due to remarkable improvements in various deposition technique like electron beam evaporation [7, 8], magnetron [9-11] and ion beam sputtering [12-14] or pulsed laser deposition [15-17], multilayers of various metal or semiconductor materials with layer thicknesses ranging down to less than 1 nm, layer numbers of many hundreds to thousands, and layer precisions in terms of thickness and interface accuracies on an atomic length scale (0.1 nm) have been realized.

While most multilayer optics development in the past was directed toward improved reflectivities for various multilayer material combinations and various photon energies from extended ultraviolet to the soft x-ray regime, and such multilayer optics have been employed as imaging devices in solar astronomy [18], extreme ultraviolet lithography [19] and microscopy [20], plasma diagnostics [21], Synchrotron Radiation optics [22] and many more, their application to the formation and handling of ultrashort soft x-ray radiation bursts with a few femtosecond (10^{-15} s) to attosecond (10^{-18} s) pulse durations, as they have become accessible since a few years by advanced laser technology in High

Alexander Guggenmos

Faculty of physics, Ludwig-Maximilians-University Munich, Am Coulombwall 1, D-85748 Garching, Germany

Harmonic Generation (HHG) [23] or advanced electron accelerator technology in Free Electron Lasers [24], has only recently been discussed in literature, however gaining increasing attention from the scientific community.

This article is a review about the status of (our) multilayer attosecond optics development in these fields.

1.1.1. Attosecond Pulses (Isolated and Pulse Trains)

Attosecond pulses of soft x-ray radiation bursts, either as isolated single pulses (where one attosecond pulse is generated by one laser pulse) or as pulse trains (where multiple about equal spaced attosecond pulses are generated by one laser pulse) have become possible by the invention of femtosecond laser amplifiers delivering few-cycle laser pulses with controlled electric field under the pulse envelope (Carrier Envelope Offset phase stabilization) and their frequency conversion in High Harmonic Generation (HHG). They constitute as of today one of the shortest electromagnetic pulses in time and provide the basis for time-resolved experiments characterizing the temporal dynamics of electron wave packets in atoms, molecules or even condensed matter systems.

While HHG is delivering extremely short pulses in time, their very small conversion efficiency limits their applicability currently to the extreme ultraviolet (lower soft x-ray) range and to very low pulse energies.

Pulses of higher photon energy in the soft- to hard x-ray range and much larger pulse energies can be delivered by Free Electron X-ray Laser sources, however their pulse duration is currently limited to some tens of femtoseconds. Very recent experiments performed at LCLS however might have an experimental way to further compress such pulses into the few femtosecond, or even sub-femtosecond, regime [25], which might then outperform current HHG sources in the foreseen future.

However, both sources in common is the generation of broad bandwidth radiation at short spectral wavelength, which requires proper handling of the spectral amplitude as well as of the spectral phase by subsequent optics components. Multilayer optics are proven to play a dominant role in controlling the amplitude and phase of the reflected radiation, thus providing a powerful toolbox for temporal pulse shaping. These properties are described in the following article.

1.1.2. HHG as Major/Only Attosecond Pulse Source

There are many publications on the generation of attosecond pulses by High Harmonic Generation, delivering a very intuitive theoretical description [26] of this process as well as describing the required experimental setups [27] and generated radiation spectra and pulses [28].

The process of HHG in atoms and molecules is theoretically best described by the three-step model of Paul Corkum [29], separating the sub-steps into laser-field induced tunnel

ionization of electrons during a fraction of laser period, followed by the acceleration of the free charges in the ponderomotive laser field, and finally the re-scattering of the returning electrons with their mother cores.

It is important to note, that this process delivers a coherent (spatially and temporally) radiation spectrum with multiple odd overtones (harmonics) of the driving laser frequency starting from the lasers fundamental wavelength (with a Ti: sapphire laser usually in the near-infrared at 780 nm) ranging over the strongly modulated and plateau area toward the weakly modulated cut-off regime, constituting the shortest HHG wavelengths.

The spectral position of the HHG cut-off is determined by the lasers pulse intensity and frequency as well as the ionization potential of the target atom and is given by the following formula:

$$E_{cut-off} = I_P + 3.17 \bullet U_P ,$$ (1.1)

with the target atom ionization potential I_P and the ponderomotive potential of the laser:

$$U_P = \frac{Ie^2}{2m_0 \varepsilon_0 c \omega_L^2} .$$ (1.2)

The forming of single isolated attosecond pulses from such broad band HHG radiation spectra is performed by filtering out the shortest-wavelength part of the HHG spectrum in the cut-off regime, which is typically achieved by transparent filter foils, grazing incidence or multilayer reflectors, or a combination of those elements.

While thin-film filters and grazing incidence optics are not very versatile for tailor-made spectral filtering and spectral phase manipulation, multilayer optics as such described herein allow for a wide range of tailor-made spectra and phases, thus providing best flexibility for temporal pulse shaping.

1.1.3. What Is It Good for? The Applications

Coherent extreme ultraviolet pulses from High Harmonic Generation and their optics components find a wide range of applications in experiments, where some make use of the almost perfect coherence of the generated radiation, such as in experiments on extreme-ultraviolet interferometry [30], HHG microscopy such as Coherent Diffractive Imaging [4], or the generation of EUV frequency combs for advanced metrology [31].

However, the majority of applications of HHG radiation utilizes the attosecond temporal structure, e.g. in pump-probe experiments on electron streaking providing insights in the electron wave packet dynamics in atoms [32] and molecules [33] as well as giving new insights in the photoemission process from solid surfaces [34] or nanostructures [35].

While most of the experiments utilize single isolated attosecond pulses, as they are required for clean electron streaking experiments, recently also the use of attosecond pulse

trains has been established in RABBITT measurements and might provide a path to attosecond angle-resolved photoemission spectroscopy (ARPES) characterization of solid surfaces in the near future [36].

It is important to note, that all those different experiments impose differing requirements on the inevitable spectral filtering of the HHG spectrum by the extreme ultraviolet optical components, which can in many cases be best achieved by proper multilayer reflectors.

1.2. Reflective Optics in the EUV/Soft X-Ray Range

1.2.1. Interaction of Radiation with Matter

The interaction of electromagnetic waves with matter can be described by the index of refraction $n = c/v_p$, where c is the speed of light and v_p is the phase velocity in the medium. The phase velocity is usually decelerated in a medium, since the electric field disturbs the charges of each atom proportional to the electric susceptibility of the medium. This disturbance decreases with increasing frequency. Fig. 1.1 illustrates the progression of the index of refraction dependent on the electromagnetic wave's frequency ω.
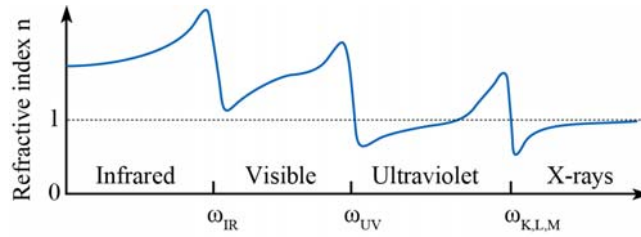

Fig. 1.1. Real part of the index of refraction as a function of the frequency with strong variations near the resonance frequencies [37].

It shows strong variations near IR, UV and x-ray resonances (ω_r) and the tendency toward unity for very short wavelengths. Only the real part of the index of refraction is shown in Fig. 1.1. Its adaption to a complex refractive index is necessary in case of attenuation in the medium. When electromagnetic waves get attenuated in a medium one considers this absorptive effect and defines the complex index of refraction as:

$$\tilde{n} = n + i\kappa ,\qquad(1.3)$$

where κ is the extinction coefficient. The real part of Eq. (1.3) approaches unity for electromagnetic waves with wavelengths in the EUV/soft x-ray range, since the dispersion of the medium strongly decreases. One considers the low dispersion background in that energy range by rewriting Eq. (1.3) to the EUV/soft x-ray form:

$$\tilde{n}(\omega) = 1 - \delta + i\beta ,\qquad(1.4)$$

with the dispersion δ and the extinction coefficient β. The influence of δ and β on the light-matter interaction becomes clear, when one considers the propagation of a plane wave in z-direction through a material with a refractive index n. The electric field can be written as:

$$E(z,t) = E_0 e^{-i(\omega t - zr)} . \tag{1.5}$$

The complex index of refraction is considered by:

$$\frac{\omega}{k} = \frac{c}{n} = \frac{c}{1-\delta+i\beta} \Leftrightarrow k = \frac{\omega}{c}(1-\delta+i\beta) . \tag{1.6}$$

Using Eq. (1.6) in Eq. (1.5) leads to:

$$E(z,t) = \underbrace{E_0 e^{-i\omega\left(t-\frac{z}{c}\right)}}_{\substack{vacuum \\ propagation}} \underbrace{e^{-i\left(\frac{2\pi\delta}{\lambda}\right)}}_{\varphi-shift} \underbrace{e^{-\left(\frac{2\pi\beta}{\lambda}\right)z}}_{decay} . \tag{1.7}$$

The first term in Eq. (1.7) describes the propagation of a plane wave through vacuum, the second term contributes a phase shift dependent on the dispersion δ and the last term is a damping term, accounting for absorption within the medium. The extinction coefficient β is related to the absorption coefficient α by squaring Eq. (1.7):

$$I = I_0 e^{-\alpha z} \Leftrightarrow \alpha = \frac{4\pi\beta}{\lambda} , \tag{1.8}$$

where I represents the Intensity and α is the inverse of the absorption length $l_{abs} = \alpha^{-1}$.

Eq. (1.4) can also be written as a function of the real part (f_1) and imaginary part (f_2) of the atomic scattering factor:

$$n(\omega) = 1 - \frac{r_e n_a \lambda^2}{2\pi}\left[f_1(\omega) - if_2(\omega)\right], \tag{1.9}$$

with the classical electron radius $r_e = e^2/(4\pi\varepsilon_0 mc^2)$ and the electron density per unit volume n_a. Comparing Eq. (1.9) and Eq. (1.4) yields the relation between the atomic scattering factor and the dispersion and extinction, respectively:

$$\delta = \frac{n_a r_e \lambda^2}{2\pi} f_1(\omega), \tag{1.10}$$

and

$$\beta = \frac{n_a r_e \lambda^2}{2\pi} f_2(\omega). \tag{1.11}$$

One can thus calculate the dispersion and the extinction by making use of the measured tabulated values of the atomic scattering factors by Henke et al. [38]. The index of refraction approaches unity due to these low values (10^{-2}-10^{-7}) where the values of δ and β are typically on the same order. This approach and the high absorption for EUV/soft x-ray wavelengths (Eq. (1.8)) results in low refraction at an interface between two materials (due to the similarity of the optical constants) and a limited penetration depth (on the order of a few hundred nm). This limits the degree of freedom of EUV/soft x-ray optics, since they must be either very thin, be used under small grazing angles in reflection geometries or use multiple reflections from different interfaces as utilized in multilayer mirrors.

1.2.2. Single Interface Reflectance (and Transmission)

One can use e.g. metal bulk mirrors for a broadband and high reflective guidance of visible light under nearly arbitrary angles of incidence. Unlike the visible range, no comparable optics can be used in the EUV/soft x-ray range. If an electromagnetic wave incidents under an angle α_i on an interface which is formed by two layers with the refractive indexes n_1 and n_2, it is usually reflected and transmitted (Fig. 1.2).
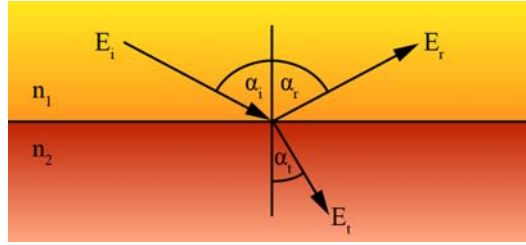

Fig. 1.2. Reflected and transmitted electric field at an interface, formed by two materials with the index of refraction n_1 and n_2.

The degree of reflection and transmission depends on the incident angle α, on the index of refraction of both media and on the polarization state s or p. The characteristics are described by the Fresnel equations [39]:

$$r_s = \frac{E_{rs}}{E_{is}} = \frac{\tilde{n}_1 \cos\alpha_i - \tilde{n}_2 \cos\alpha_t}{\tilde{n}_1 \cos\alpha_i + \tilde{n}_2 \cos\alpha_t}, \tag{1.12}$$

$$t_s = \frac{E_{ts}}{E_{is}} = \frac{2\tilde{n}_1 \cos\alpha_i}{\tilde{n}_1 \cos\alpha_i + \tilde{n}_2 \cos\alpha_t}, \tag{1.13}$$

$$r_p = \frac{E_{rp}}{E_{ip}} = \frac{\tilde{n}_2 \cos\alpha_i - \tilde{n}_1 \cos\alpha_t}{\tilde{n}_1 \cos\alpha_t + \tilde{n}_2 \cos\alpha_i}, \tag{1.14}$$

$$t_p = \frac{E_{tp}}{E_{ip}} = \frac{2\tilde{n}_1 \cos\alpha_i}{\tilde{n}_1 \cos\alpha_t + \tilde{n}_2 \cos\alpha_i} \,. \qquad (1.15)$$

Here, r and t are the reflection and transmission coefficients, respectively and E represents the complex electric field amplitude, while the indices determine the polarization (s or p) and whether the incident (i), the reflected (r) or the transmitted (t) fraction is considered. The different index of refraction is considered by n_1 and n_2. Throughout this article, normal incidence angles are referred to as α and grazing angles as θ. The single interface reflectance for angles much larger than the critical angle θ_c ($\theta = 90° - \alpha$) can be approximated to:

$$R_{1,2} = \frac{\Delta\delta^2 + \Delta\beta^2}{4\cos^4(\alpha_i)} \,, \text{ for } \beta \ll \delta \ll 1, \theta \gg \theta_c \left(\sin\theta_c \approx \sqrt{2\delta}\right). \qquad (1.16)$$

Summarized, the single interface reflectivity is given by the difference of the optical constants of both media and the normal incidence angle α_i and is a rather low value in the EUV/soft x-ray wavelengths range.

1.2.3. Multilayer Mirrors

Multilayer mirrors address the issue of low single interface reflectivity as was described in the previous section. Creating a stack of alternating layers of varied materials makes use of constructive interference of partially reflected electromagnetic waves at each interface. Dependent on the working energy range and bandwidth 10-1000 interfaces are utilized. Each single interface reflectivity is still small but adding up each interface reflectivity can result in a normal incidence EUV reflectivity above 70 % [6] near the Si L3-edge. Constructive interference of the waves reflected at each interface can be achieved by a proper material choice and thickness design yielding a tailored reflectivity characteristic. This allows for a very precise spectrally filtering and shaping of attosecond pulses. Multilayer can be coated on arbitrary surfaces which allows for various shapes like parabolas, ellipsoids or the most commonly used spheres. Summarized, multilayer mirrors can tailor attosecond pulses and can be used for beam guidance, imaging or focusing and stand out as key components in attosecond science. The development of multilayer mirrors for the EUV started in the 1970s [5], it also pushed the development in the VIS/IR as the EUV range is more challenging and achieved results in that energy range can be easily adapted to the VIS/IR range. Nowadays it's state-of-the-art in the VIS/IR range to calculate [40] or even realize [41] very complex designs by the usage of various techniques [42, 43] and fulfill different requirements such as enough photon throughput or dispersion control at the same time [44]. This development and its results were extended to the EUV/soft x-ray range in the last years for various applications such as soft x-ray microscopy [20], EUV lithography [19], astronomy [18] or time resolved attosecond spectroscopy [45]. The last-mentioned attosecond science will be extended from the EUV range to the soft x-ray water window range in the near future.

1.2.3.1. Principal of Multilayer Mirrors

In Section 1.2.2 the reflectance and transmission of a single interface was described. This is now extended to a multilayer system, where multiple interface reflections and transmissions occur. One starts with the j-th layer within a stack consisting of one interface at the top and one at the bottom. The corresponding reflection coefficient reads as:

$$r_j = r_{(j-1)j} + t_{(j-1)j}t_{j(j-1)}r_{j(j+1)}e^{-2i\varphi_j} + t_{(j-1)j}t_{j(j-1)}r_{j(j-1)}r_{j(j+1)}^2 e^{-4i\varphi_j} + \ldots, \quad (1.17)$$

where r and t are the reflection and transmission coefficients, respectively. Their indices determine at which interface the reflection and transmission occurs. The phase difference between the waves reflected at the bottom and the top interface is referred to as φ_j and can be written as:

$$\varphi_j = \frac{2\pi d_j}{\lambda} n_j \sin\theta_j, \quad (1.18)$$

where n_j is the index of refraction and θ_j the angle of incidence of the j-th layer. Fig. 1.3 illustrates all these parameters.
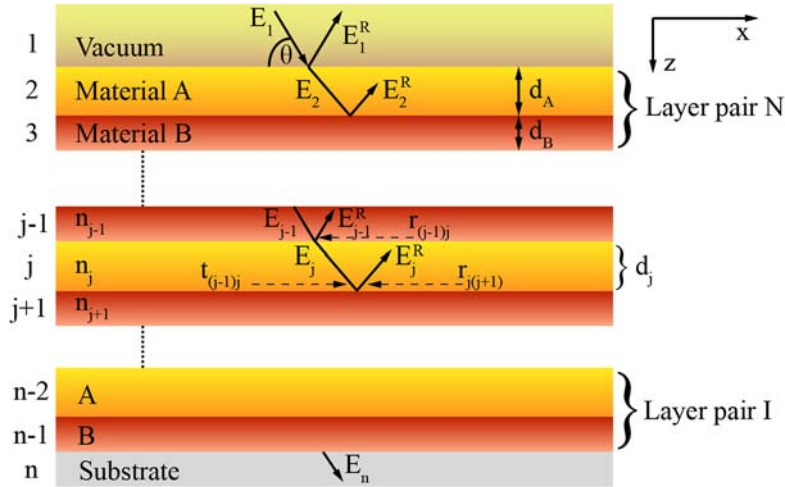

Fig. 1.3. Principle of multiple reflections and transmissions within a multilayer stack. The incident electromagnetic wave is partly reflected and transmitted at each interface (figure is related to [46]).

The sum in Eq. (1.17) converges to [47]:

$$r_j = \frac{r_{(j-1)j} + r_{j(j+1)}e^{-2i\varphi_j}}{1 + r_{(j-1)j}r_{j(j+1)}e^{-2i\varphi_j}}. \quad (1.19)$$

With this recursive formula, one can calculate the reflectivity of the overall multilayer stack. One starts from the lowermost layer of the stack, where the reflectivity is given by the single interface reflectivity of the substrate, and the first layer, and 'walks' through the stack. The reflectivity is calculated layer by layer and one ends up with the overall reflectivity $r_{ML} = r_1$. Its intensity is given by $R = |r_1|^2$.

1.2.3.2. Periodic and Aperiodic Multilayer Systems

The main classification for multilayer mirrors is to distinguish between periodic and aperiodic systems. Periodic mirrors usually consist of two (three) varied materials in alternating order where one usually refers to the low absorbing material as *spacer* whereas the high absorbing material as *absorber*. Aperiodic multilayer systems have individual layer thicknesses without any periodicity. Periodic stacks are characterized by the following parameters:

- The period thickness d which is constant throughout the stack.

- The period number N is the number of bilayers (trilayers) in a two (three) material stack. In a more general way: How often is the period used within a stack ?

- The fraction of the different layer thicknesses within one period, denoted as γ ratio. In a two-material stack: $\gamma = d_{bottom}/d \leftrightarrow d_{top}=d(1-\gamma)$. In the case of more than two materials per period one defines one γ_A per material A.

Fig. 1.4 illustrates a typical Gaussian like reflectivity and flat phase (within the bandwidth) shape of a periodic multilayer mirror.

The characteristic values such as maximum reflectivity, center energy or bandwidth are influenced by the listed multilayer parameters.
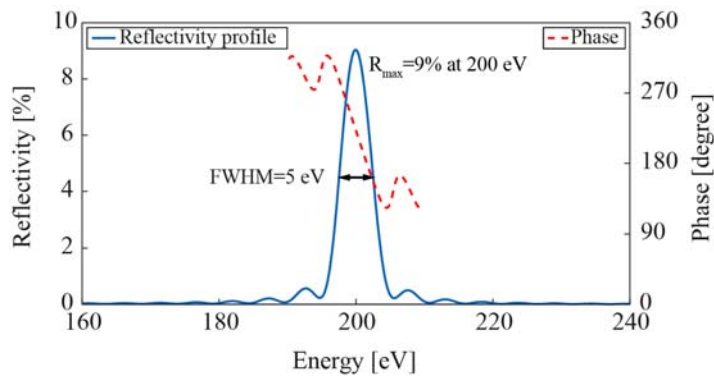

Fig. 1.4. Reflectivity and phase shape of a periodic multilayer mirror. Simulated reflectivity (solid blue) and phase (dashed red) of a periodic Cr/Sc multilayer mirror. Following parameters have been used for the simulation: spacer Sc, absorber Cr, d = 3.144 nm, γ = 0.6, d_{Sc} = 1.886 nm, d_{Cr} = 1.258 nm, N = 37, α = 5°.

The period thickness determines the center wavelength of the mirror according to the modified Bragg equation accounting for refraction:

$$m\lambda = 2d \cdot \sin\theta \sqrt{1 + \frac{\bar{n}^2 - 1}{\sin^2\theta}} \, , \qquad (1.20)$$

where m is the diffraction order, λ is the wavelength of the incident light, θ is the grazing angle and n the mean real part of the complex refractive index including the averaged dispersion within one period d consisting of k materials:

$$\bar{\delta} = \sum_k \frac{d_k \delta_k}{d} \, , \qquad (1.21)$$

where d_k is the individual layer thickness and δ_k the corresponding dispersion within the period thickness d. The square root in Eq. (1.20) takes refraction effects into account and is sometimes neglected at normal incidence as the denominator approaches unity and $n \approx 1$. Neglecting the square root in Eq. (1.20) yields the condition for maximum normal incidence reflectivity: the optical period thickness is equal to $\lambda/2$, i.e. $d \approx 6$ nm at 100 eV.

The period number N influences the overall reflectivity, since more contributing layers increase this value, but its continuous increment is limited by the absorption of the materials. At the point of saturation more periods will not contribute to the overall reflectivity. The number of contributing periods can be increased by adapting the gamma ratio for reducing the amount of absorbing material. But this procedure is limited in case of mirrors for attosecond pulses. For the support of attosecond pulses the reflectivity is a very important factor but comes always along with the pulse duration support. This point is linked by the bandwidth support and can be approximated by the multilayer parameters by:

$$\frac{\Delta\lambda}{\lambda} = \frac{\Delta E}{E} \approx \frac{1}{mN} \, , \qquad (1.22)$$

where m is the diffraction order. The bandwidth is linked to the support of the temporal pulse duration by

$$\Delta E[eV] \bullet \tau_0[as] \approx 1824[eV \bullet as] \, , \qquad (1.23)$$

which is known as the time-bandwidth product and is a result of the Fast Fourier Transform (FFT) of a Gaussian pulse and its full width at half maximum (FWHM) consideration.

Periodic multilayer mirrors have an almost linear phase within the bandwidth, since the strong periodicity ensures that each period contributes equally throughout the stack. Consequently, periodic multilayer mirrors do not temporal broaden an incoming pulse, but are therefore also not able to compress an incoming pulse. The influence on pulse shaping is limited by periodic systems.

A higher degree of freedom for attosecond pulse shaping is achieved by utilizing aperiodic multilayer mirrors in contrast to periodic stacks. While each period is equal in a periodic stack, i.e. the thickness for a certain material is constant, the thicknesses are arbitrary [46] in an aperiodic stack. This facilitates addressing different frequency components by individual layer thicknesses. This allows for spectral and dispersion shaping as different frequency components are reflected at different penetration depths within the stack. Fig. 1.5 illustrates the principle of aperiodic multilayer stacks.

In Fig. 1.5 (a) longer wavelengths are reflected on the top whereas short wavelengths are reflected at the bottom. Therefore, the short wavelengths are temporally delayed in respect to the longer wavelengths due to the longer penetration distance. This is defined as positive chirp; the mirror introduces a positive group delay dispersion (GDD). Vice versa in case of a negative chirp (Fig. 1.5 (b)). This facilitates shaping the dispersion of an incoming attosecond pulse and tailoring the reflected pulse. Aperiodic multilayer systems in the visible/infrared spectral range (e.g. (dielectric) multilayer mirrors in 'chirped pulse amplification' (CPA) systems) show an almost linear decreasing or increasing (dependent on the introduced GDD) of the layer thicknesses [41], due to missing absorption in dielectric materials in this spectral range, whereas aperiodic EUV/soft x-ray multilayer mirrors exhibit usually a random stack arrangement. Therefore Fig. 1.5 reflects only a useful presentation of delaying different wavelengths at different penetration depths, a real multilayer stack design for the EUV differs from this presentation, since the influence of strong absorptions leads to a rather random like stack design, which can be seen in the next figure. Fig. 1.6(a) depicts the design of a complex aperiodic multilayer stack consisting of 48 different layers and five varied materials ($MoSi_2$ is formed after deposition [48]).
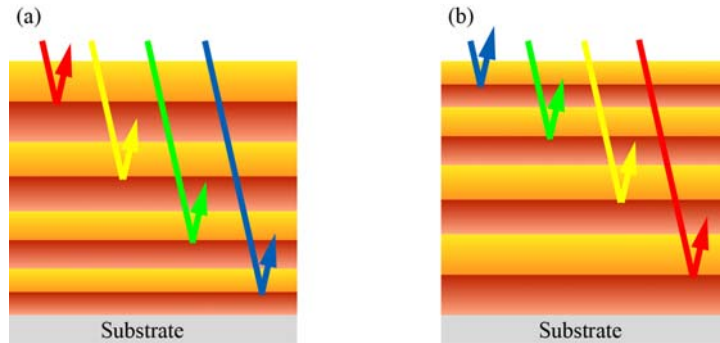

Fig. 1.5. Aperiodic multilayer stack. Sketch of aperiodic multilayer stacks, where different wavelengths are reflected at different penetration depths. The almost linear decreasing/increasing of the layer thickness is used for the VIS/IR range whereas it is rather a random stack arrangement in the EUV/soft x-ray range. (a) A positively chirped multilayer stack where short wavelengths are temporally delayed in respect to the longer wavelengths due to the longer penetration distance; (b) Vice versa in case of a negatively chirped mirror.

This complex design has been developed for the reflection of a FWHM>40 eV and a close to Gaussian spectral profile, when it is convoluted with the transmission of a 150 nm thick

Pd filter (Fig. 1.6 (b)). A periodic stack supporting a bandwidth of 40 eV at 145 eV would, according to Eq. (1.22), have only four periods. That are eight layers in contrast to the 48 layers of the aperiodic system. This demonstrates why aperiodic multilayer mirrors exhibit a much higher degree of freedom in contrast to periodic stacks. Besides, one would expect that eight layers of the periodic case have a lower overall reflectivity as only a sixth of the aperiodic interface number is used. This is another advantage of aperiodic multilayer mirrors in addition to dispersion control. One can e.g. increase the reflectivity of a periodic system by switching to an aperiodic design while keeping the bandwidth constant.
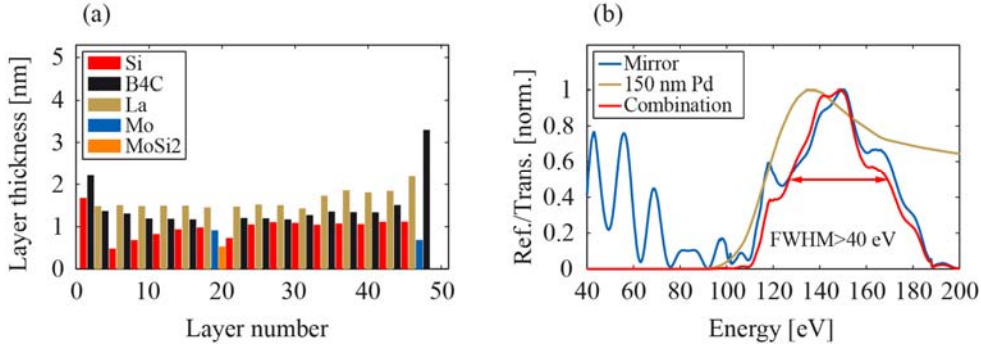

Fig. 1.6. A complex aperiodic La/Mo/Si/B4C mirror design: (a) Design of a complex aperiodic multilayer consisting of 48 different layers and five varied materials; (b) Reflectivity (blue), transmission of a 150 nm thick Pd filter (brown) and their convolution (red) resulting in a bandwidth of more than 40 eV. A normal incidence angle of 5 degree and a constant interface roughness of $\sigma = 0.5$ nm was assumed for the simulation.

1.2.3.3. Imperfect Interfaces

It is impossible to realize multilayer mirrors with perfectly abrupt and flat interfaces as finite boundaries occur during the fabrication. Interface imperfections are mainly caused by interface roughness [39] from fringed interfaces (Fig. 1.7 (a)) or atomic displacement as intermixing or interdiffusion (Fig. 1.7 (b)).
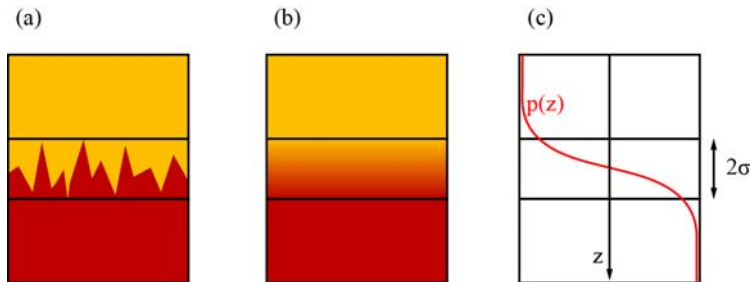

Fig. 1.7. The interface roughness σ: (a) Corrugated interface, (b) Intermixing and interdiffusion of both materials, (c) Interface profile function $p(z)$ for modeling both boundary imperfections.

Also, chemical reactions are possible forming an interlayer, as can be observed in Mo/Si multilayer where thin $MoSi_2$ layers are formed [48, 49]. This interlayer can be considered by including an additional layer with the corresponding refractive index of the compound. One should find a way to model these described imperfections and include it in simulations of multilayers, since it will be shown that they have a crucial effect on the reflectivity performance. This is mathematically done by the interface roughness value σ. One could now include the transition zone in simulations by representing the interface by a stack of very thin layers of continuously varying refractive index [39], but this would be a very time-consuming calculation especially when more than two materials are used or aperiodic stacks with a large layer number are simulated. Debye [50] and Waller [51] developed a rather elegant model to implement the roughness via Fourier transformation. An interface profile function p(z), like the one-dimensional error function, is used to characterize the interface width for both roughness and diffusion (Fig. 1.7(c)):

$$p(z) = erf\left(\frac{z}{\sqrt{2}\sigma}\right), \tag{1.24}$$

with the one-dimensional Gauss error function erf(x) and its FWHM σ. Using this profile function the reflection coefficient of the interface can be written as a Gaussian distribution:

$$r(z) = \frac{r_0}{\sigma\sqrt{2\pi}} e^{-z^2/(2\sigma^2)}. \tag{1.25}$$

A Fourier transformation of Eq. (1.25) yields the reflection coefficient in the momentum space:

$$r(q) = r_0 e^{-\frac{q^2\sigma^2}{2}} = r_0(\lambda)\exp\left(-\frac{8\pi^2 n^2 \sin^2(\theta)\sigma^2}{\lambda^2}\right), \tag{1.26}$$

with the wavelength dependent Fresnel coefficient $r_0(\lambda)$, the amplitude reflectivity of a perfectly abrupt boundary, and the momentum transfer $q = 4\pi n\sin(\theta)/\lambda$ between the boundary and the photon. Névot and Croce extended this method of Debye and Waller to an even more realistic description [52], considering the different refractive indices n and the resulting different propagation grazing angles θ of material 1 and material 2:

$$r(\lambda) = r_0(\lambda)\exp\left(-\frac{8\pi^2 n_1 n_2 \sin\theta_1 \sin\theta_2\sigma^2}{\lambda^2}\right). \tag{1.27}$$

The Névot-Croce model is used for all simulations within this article to account for interface imperfections. Squaring Eq. (1.27) yields the intensity dependence:

$$R = R_0 \exp\left[-n_1 n_2 \sin\theta_1 \sin\theta_2\left(\frac{4\pi\sigma}{\lambda}\right)^2\right]. \tag{1.28}$$

The influence of roughness on the reflectivity performance of a multilayer mirror for attosecond pulses is shown in Fig. 1.8.

The two plots of Fig. 1.8 are simulations of a molybdenum/silicon multilayer mirror ($N = 26$, $d = 6.7$ nm, $\gamma = 0.4$, $\alpha = 5°$), including no molybdenum silicide layers, with a bandwidth of 5 eV in case of no interface roughness. According to Eq. (1.23) this would support ~400 as pulses. Eq. (1.28) has shown that an increased roughness value reduces the overall throughput, which is simulated in Fig. 1.8(a). Due to an increased diffuse scattering, this is accompanied by a decrease of the supported bandwidth. This is directly linked to the supported pulse duration, which is increased ($\sigma = 0$ nm supports a FWHM of 5 eV and thus ~400 as pulses whereas in case of $\sigma = 1.5$ nm only a bandwidth of 3.2 eV is possible resulting in a pulse duration support of ~600 as). Summarized a bad interface roughness reduces the overall photon throughput and increases the supported pulse duration. In terms of attosecond pulses both criteria are important and consequently the interface roughness should be minimized.
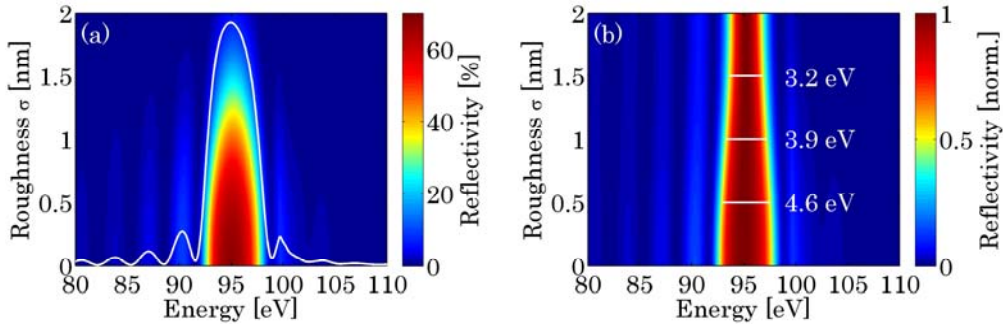

Fig. 1.8. (a) The influence of interface roughness σ on the reflectivity for a typical MoSi multilayer system for different σ values. The lineout indicates the reflectivity profile for $\sigma = 0$ nm (the reflectivity colormap is used as y-axis for the lineout); (b) Normalized reflectivity for each roughness value to demonstrate the decrease of bandwidth with increasing roughness.

1.3. Simulations of Multilayer Systems - Their Theoretical Optical Performance

For reflectivity and transmission calculations we use a self-written multilayer Fresnel code algorithm written with the software MATLAB. The overall reflectivity (mirror) or transmission (polarizer, filter) is calculated together with the relevant phase based on the multiple interface reflections and transmissions described in Section 1.2.3.1. The code uses the tabulated values of the atomic scattering factors from Henke and Gullikson [38] above 30 eV to calculate the dispersion (Eq. (1.10)) and the extinction (Eq. (1.11)) necessary for the Fresnel equations of Section 1.2.2. Realistic imperfect interfaces (Section 1.2.3.3), top layer oxidation or interlayer formation like molybdenum silicide [53] are considered as the stack design demands. We can thus identify various parameters which are used as input for the simulations. These parameters are either tabulated from

former characterization measurements or theoretical studies or should be extracted from own research studies and different characterization or analysis methods:

- **The optical constants.** Tabulated like Henke and Gullikson [38], updated self-determined tabulated values at certain absorption edges [54] or directly measured by spectral ellipsometry [55] for performance approximations in other spectral ranges.

- **Realistic interface roughness values.** Extracted from soft [56] or hard x-ray reflectometry [57] measurements as well as cross section transmission electron microscopy [58].

- **Top layer oxidation.** Analysis methods like for the roughness and additionally spectral ellipsometry. The thickness loss of the top material as well as the thickness of the grown oxide layer should be determined, since those two layers are responsible for a small aperiodicity within the stack as well as those are the first layers the radiation penetrates through, a very important fact in case of EUV radiation.

- **Interlayer formation.** Analysis methods like for the roughness.

The self-written code is used for simulating the optical performance of periodic multilayer systems or of already calculated aperiodic designs. The calculations of aperiodic designs are previously realized with the software *Optilayer*, a Fresnel code coupled to a 'needle optimization' algorithm [42, 43]. This software is used for the optimization (mainly chirped mirrors) of multilayer systems in combination with the self-written Fresnel code. The most important prerequisite for a reasonable optimization is the properly chosen start design. One usually starts with a periodic multilayer system which consists of the material combination best suitable for the aimed spectral range and adjusts the layer thicknesses (optimized γ-ratio) to the central energy E of interest. The period number N of the start design is chosen according to the required spectral bandwidth E and is estimated by:

$$N = \frac{E}{\Delta E} . \tag{1.29}$$

Finally, one defines one or more target functions for the algorithm for which the start design should be optimized. The optimization can, for example, include a higher peak reflectivity, a spectral broader mirror reflectivity or in case of chirped mirrors an optimized spectral phase being realized by aperiodic layers, thus introducing a group delay dispersion in contrast to a flat phase in case of a periodic system. The needle optimization algorithm [42] starts with the periodic design and inserts small needlelike additional layers at certain positions in the stack, defined by the best benefit for the merit function. The thicknesses of these layers are consecutively increased or decreased until their best thickness value is achieved. Each optimization procedure consists of a certain number of iterations in which the current design is changed by random walk within user defined limits. The quality of a design $D_i(\omega)$ is quantized by the merit function MF including weights w_i (which must be predefined) that define the importance of the individual target function $T_i(\omega)$.

$$MF = \sum_i w_i \left[D_i(\omega) - T_i(\omega) \right]^2. \tag{1.30}$$

The figure-of-merit function further rules whether the modern design is taken as start design for the next iteration step or not. Thus, every calculated design is a trade-off between different target functions and is a consequence of the start design. Finally, the implementability of a final design should be checked and converted into deposition times using a self-written Fresnel-code algorithm. Interlayer formation, structural changes yielding thickness losses and a realistic Névot-Croce roughness is included in the code and both the spectral and the temporal structure of the pulse is analyzed including both the source and the filter characteristics to be able to compare the most realistic pulse simulation with the experimental constraints. Ultrathin layers because of the needle optimization procedure are either eliminated or broadened to a realizable value of at least 1 nm. If the final design does not fulfill the earlier formulated requirements an innovative design optimization is necessary either with a better start design or fresh design target points and weights. This procedure is used for aperiodic multilayer mirrors for shaping attosecond pulses.

1.4. Fabrication of Multilayer Coatings

Multilayer coatings are realized by various deposition techniques. Every technique has advantages and disadvantages and one should evaluate the coating priorities according to numerous criteria such as overall cost, deposition speed, layer density (which is directly connected to damage thresholds), thickness accuracy, number of target materials, availability of target materials, vacuum requirements, in-situ characterization techniques, coating homogeneity, to name only some of them. Nowadays following techniques are used for the realization of multilayer coatings:

- **Electron beam physical vapor deposition (EBPVD)** [7, 8], is a form of physical vapor deposition in which a target anode is bombarded with an electron beam given off by a charged tungsten filament under high vacuum. The electron beam causes atoms from the target to transform into the gaseous phase. These atoms then precipitate into solid form, coating everything in the vacuum chamber (within line of sight) with a thin layer of the anode material.

- **Magnetron sputtering** [9-11] is a Plasma Vapor Deposition (PVD) process in which a plasma is created and positively charged ions from the plasma are accelerated by an electrical field superimposed on the negatively charged electrode or 'target'. The positive ions are accelerated by potentials ranging from a few hundred to a few thousand electron volts and strike the negative electrode with sufficient force to dislodge and eject atoms from the target. These atoms will be ejected in a typical line-of-sight cosine distribution from the face of the target and will condense on surfaces that are placed in proximity to the magnetron sputtering cathode.

- **(Dual) ion beam deposition (D-IBD)** [12-14] apparatus typically consists of an ion source, ion optics and the deposition target. Optionally a mass analyzer can be incorporated. In the ion source, materials in the form of a gas, an evaporated solid, or a solution (liquid) are ionized. The ions are then accelerated, focused or deflected using high voltages or magnetic fields. Optional deceleration at the substrate can be employed to define the deposition energy. This energy usually ranges from a few eV up to a few keV. At low energy, molecular ion beams are deposited intact (soft landing), while at a high deposition energy molecular ions fragment and atomic ions penetrate further into the material, a process known as ion implantation. The ion beam current, which is quantitative measure for the deposited amount of material, can be monitored during the deposition process.

- **Pulsed laser deposition (PLD)** [15-17] is a physical vapor deposition (PVD) technique where a high-power pulsed laser beam is focused inside a vacuum chamber to strike a target of the material that is to be deposited. This material is vaporized from the target (in a plasma plume) which deposits it as a thin film on a substrate. This process can occur in ultra-high vacuum or in the presence of a background gas, such as oxygen which is commonly used when depositing oxides to fully oxygenate the deposited films.

- **Metalorganic vapor phase epitaxy (MOVPE)**, also known as organometallic vapor phase epitaxy (OMVPE) or metalorganic chemical vapor deposition (MOCVD) [59, 60], is a chemical vapor deposition method used to produce single or polycrystalline thin films. It is a highly complex process for growing crystalline layers to create complex semiconductor multilayer structures. In contrast to molecular beam epitaxy (MBE) the growth of crystals is by chemical reaction and not physical deposition. This takes place not in a vacuum, but from the gas phase at moderate pressures (10 to 760 Torr). As such, this technique is preferred for the formation of devices incorporating thermodynamically metastable alloys, and it has become a major process in the manufacture of optoelectronics.

1.5. Achieved Results and Examples for Attosecond Multilayer Mirrors

This section will aim on the results which have been achieved so far in different spectral ranges. Ever shorter isolated attosecond pulses enable experimental access of absolute or relative timing of electronic processes with never achieved temporal resolution [26, 61, 62]. The filtering, reflection and shaping of attosecond pulses requires phase-correct broadband optics. Especially in normal incidence setups, the question of the shortest possible attosecond pulses is thus directly connected to the availability of appropriate optics, namely EUV multilayer mirrors and filters. One can estimate the bandwidth ΔE of an N-period multilayer stack with central energy E from Eq. (1.29): $\Delta E/E = 1/N$. An interference coating consists of at least two periods ($N \geq 2$), thus in principle, the maximum bandwidth of a periodic multilayer mirror is about half its central energy. Higher central energies relax the constraints on the bandwidth of optics and thus enable shorter reflected pulses but suffer usually from lower reflectivity.

1.5.1. A Normal Incidence Broadband 30-60 eV Mirror

Many attosecond experiments are performed in the spectral range between 30 eV and 60 eV, which is easy to access with HH sources [63-65]. The shortest attosecond pulses in this spectral range could be generated by *polarization gating*. Sansone et al. realized 130 as long pulses around 40 eV [64]. This and other experiments may benefit from broadband normal-incidence EUV optics suitable for attosecond beam guidance and focusing. An aperiodic broadband mirror reflecting between 35 eV and 50 eV with a reflectivity up to 20 % has been designed and published by Morlens et al. [66]. The here presented periodic Si/Sc mirror, centered at nearly the same central energy of ≈ 40 eV exceeds the bandwidth of Morlens' mirror by far. Its design is chosen such that the high single interface reflectivity of Si and Sc is extended by an appropriate quarter-wave design to a bandwidth of more than 20 eV. Until now, Sc/Si multilayers have mainly been used at energies between 25 eV and 35 eV [67] just below the Sc $M_{2,3}$-edge. Above this energy, both Sc and Si are highly absorbing, and the number of contributing periods in Si/Sc multilayers is very limited. The normal incidence reflectivity saturates between 35 eV and 45 eV for only ≈ 5 periods. The relatively high reflectivity between 5-7 % is mostly independent from the mirror design due to a high single interface reflectivity of about 2 %. This property has been utilized for the design of the following ultrabroadband mirror. Its design is chosen such that the already high Si, Sc reflectivity is extended on the high energy side for a larger overall bandwidth. A 10 period Sc/Si coating with a period thickness of 14 nm (for a central energy of ≈ 50 eV) has been chosen (Fig. 1.9 (b)).
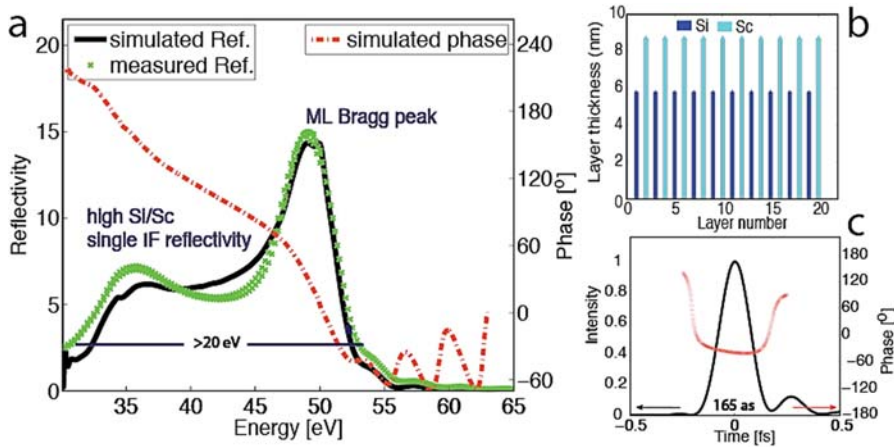

Fig. 1.9. Broadband normal incidence EUV multilayer mirror between 30 eV and 55 eV. Panel a): simulated (black) and measured (green) EUV reflectivity and spectral phase (red dash-dotted line). An σ = 1.3 nm has been used in the simulation. Panel b) shows the appropriate design of the 10 periods, d = 14 nm, γ = 0.4 Si/Sc stack. Panel c): Temporal structure of the mirror calculated as the Fourier transform of its spectral shape: It supports the reflection of 165 as sub-2 cycle EUV pulses.

Its designed and measured reflectivity is plotted together with the calculated phase in Fig. 1.9 (a). The measured EUV reflectivity confirms a successful implementation, a bandwidth of more than 20 eV and a reflectivity between 5 and 15 %. Simulations show

that this mirror is capable to support the reflection of Fourier limited 165 as long pulses what corresponds to only 1.7 EUV field oscillations at 42 eV central energy (Fig. 1.9 (c)). This mirror thus allows for the phase correct reflection of sub-2 cycle EUV pulses and is therefore at the possible duration limit at this energy.

1.5.2. Short Pulses in the 60-100 eV Range

Shorter pulses require even more bandwidth and thus necessarily higher central energies. The development of ultra-broad HH cutoff spectra with sufficiently high photon flux in the spectral range between 60 eV and 100 eV and the availability of appropriate thin metal filters and broadband high-reflectivity multilayer optics suggest this energy range for the generation of ever shorter ultrashort pulses. The HH generated EUV cut-off spectrum at about 100 eV matches the high reflectivity spectral band of Mo/Si multilayer mirrors; this material combination has thus been chosen. The generation of 80 as long pulses [68] requires at least 25 eV (FWHM) bandwidth (for a Gaussian spectrum) and is given by a multiplication of both the spectrum of the optics and the HH spectrum, from which the single pulse is being filtered. As will be presented in the following paragraph, this requires a HHG spectrum which exceeds the chirp-free cut-off region, ranging to the lower energy plateau region which is known to be positively chirped. This phase behavior (positive chirp at low energies, negligible chirp at high energies) exactly opposes that of a thin Zr filter, used in this experimental set-up anyway to filter the laser light from the EUV propagation path. As the filter indispensably compensates most of the HHG chirp, a chirp-less but broadband attosecond mirror is required. The penetration depth and thus the maximum number of usable bi-layers is limited by the attosecond pulse-length. A four-layer Mo/Si EUV coating centered at 70 eV, with a bandwidth of 32 eV (FWHM) has been designed for the coating of the inner part of the double mirror (Fig. 1.10(b)). Its reflectivity has been measured (green stars in panel a) and is in good agreement with simulations. Fig. 1.10 concludes the spectral (panel a)) and the temporal (panel c)) characteristics of this bandpass.

Simulations reveal that the mirror alone supports the reflection of nearly Fourier-limited pulses of 64 as (Fourier limit of the mirror: 63 as) calculated from the simulated spectrum (black line in Fig. 1.10 (c)) and the phase (red dash-dotted line). The effective bandpass bandwidth is experimentally limited by the transmission of the Zr filter which is required for suppression of the IR laser light and to tune the spectral phase. Different filter thicknesses (150, 300 and 450 nm) allow for some tunability of the GDD for the sake of reducing the effective bandwidth (the peak of the multiplied spectrum, plotted by the blue dashed line is shifted toward higher energies). It turned out that the combination of the mirror with a 300 nm Zr filter (yellow line, Fig. 1.10 (a)) compresses the incoming pulse to almost its Fourier limit. The goodness of the perfect interplay between the spectral phase of the bandpass and that of the HH source becomes more obvious, when one compares the temporal structure of the bandpass (panel c), blue dashed line) with its Fourier limit (light green dash-dotted line). The bandpass has a Fourier limit of 80 as, its temporal structure reveals 90 as including the phase (pulse broadening can be almost completely related to the phase of the filter). The final pulse-length of 80 as thus is at exactly the Fourier-limit of the bandpass. Please note here, that the final pulse is a

convolution of the bandpass and the incoming pulse. The HH intensity decreases at higher energies in the cut-off range and yields a slight down shift and a slight broadening of the bandpass spectrum. This experiment resulted in the generation of light flashes of no more than 80 as and has been published by E. Goulielmakis et al. in Science [68].
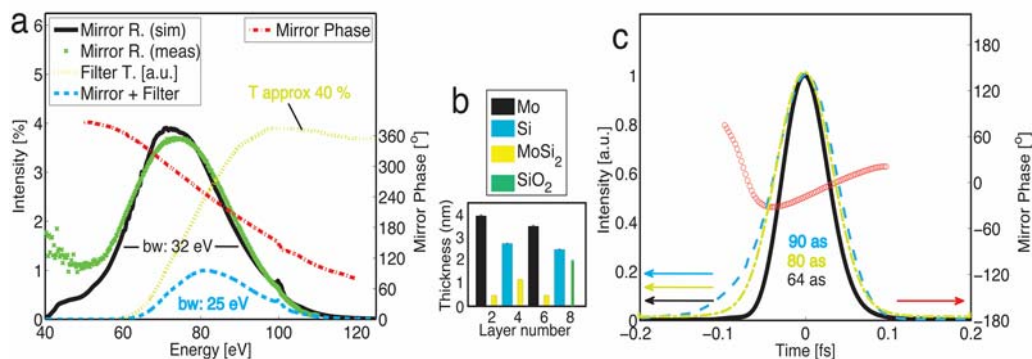

Fig. 1.10. Panel a): Simulated (black line) and measured (green crosses) reflectivity of a 32 eV (FWHM) bandwidth flat phase (red dash dotted line) multilayer mirror (design plotted in panel b), revealing a measured 3.6 % reflectivity centered at 70 eV. Together with a 300 nm thick Zr filter (yellow dotted line) it functions as a 25 eV broad bandpass and compressor (blue dashed line) for the generation of 80 as EUV pulses. Panel c shows the simulated 64 as long pulse (black line) and the temporal phase (red circles) of a pulse supported by the mirror upon reflection as an outcome of Fourier transforming the mirrors spectrum. The blue dashed line shows the temporal structure of the bandpass (mirror + filter), resulting in a 90 as long pulse, compared to its Fourier limit (light green dash dotted line) of 80 as.

1.5.3. Above the Silicon L-Edge in the 100 eV – 150 eV Photon Range

Various multilayer mirrors have been realized for attosecond pulses above 100 eV [69, 70] going from the EUV spectral range to the soft x-ray range for addressing more core states of numerous elements. The next section will describe as examples the attosecond dispersion control by multilayer mirrors, based on Hofstetter et al. [71], as well as a chromium/scandium mirror designed for a central energy around 145 eV and reflecting attosecond pulses on the order of 600 attoseconds. The later experiment was at that time realized at a central energy which was 27 eV higher than the recent energy limit in table-top attosecond pump studies [34].

1.5.3.1. Attosecond Dispersion Control by Multilayer Mirrors above 100 eV

Specially designed aperiodic binary or ternary multilayer-coated EUV mirrors allow for a large degree of freedom in influencing the EUV pulse characteristics by reflection of those mirrors [72]. So far, multilayer mirrors in attosecond physics applications were used as band-pass reflectors preserving the spectral phase of the attosecond pulse that is defined in the generation process and by the dispersion characteristics of all EUV optical elements passed by the pulse. In this work we demonstrate, how specially designed non-periodic

multilayer EUV mirrors furnish attosecond technology with the ability to control the spectral phase in addition to spectral intensity of attosecond pulses, offering a great degree of freedom in influencing the EUV pulse characteristics, such as the pulse shape, duration, frequency sweep and central wavelength.

To prove the validity of the concept for precision chirp control of attosecond EUV pulses, a set of three multilayer mirrors exhibiting distinctly different GDD but similar reflectivity characteristics was developed [71]. Optimized for an incident angle of 45° they exhibit high reflectivity within the range of 100-130 eV with comparable full widths at half maximum energy bandwidth: $\Delta E = 11\text{-}13$ eV FWHM and peaking at different central energies within the range of 107-122 eV.

The multilayer designs have been calculated and optimized by a Fresnel equation thin film code coupled to a needle optimization algorithm [42]. The mirrors have been designed such, that the GDD is almost maximum and mostly linear within the final attosecond pulse spectrum. Small shifts of the mirror spectrum due to the thin metal filter or the shape of the high harmonic cut-off spectrum have been estimated and considered in the design. The calculated designs have been optimized for additional suppressed reflectivity contributions in the near vicinity of the main Bragg peak and have been tested for stability against small layer thickness deviations. The final multilayer coating designs are displayed in the lower panels (d-f) of Fig. 1.11.
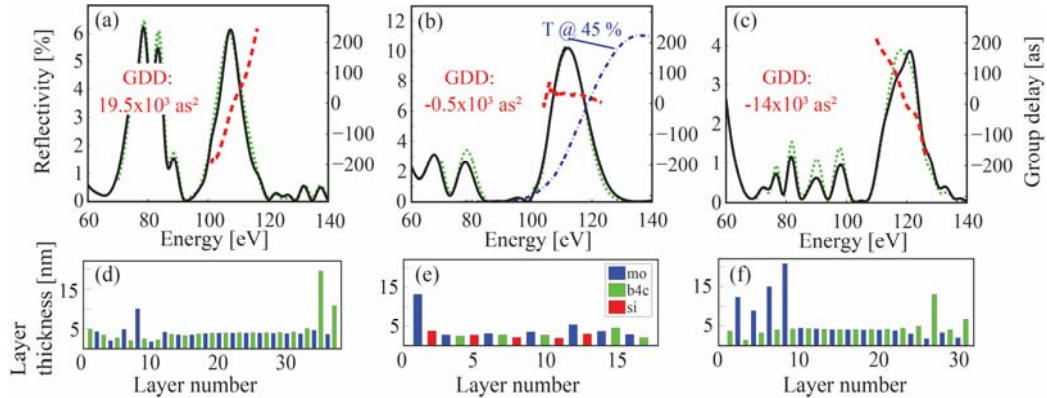

Fig. 1.11. Characteristics of EUV chirped multilayer coatings designed and manufactured for the experiments: Set of EUV multilayers with positive (a), near zero (b) and negative (c) group delay dispersion. The diagrams compare the measured (solid black) with the designed (dotted green) reflectivity curves. The calculated group delays (derivative of the spectral phase with respect to angular frequency) are also displayed (dashed red curve). The transmittivity of a 150 nm palladium foil is additionally qualitatively plotted in panel (b), depicted by the blue dash-dotted line. The lower panels (d), (e) and (f) show the corresponding mirror-designs of the appropriate mirrors above. Each color represents one material as explained by the legend in 1.2 (e).

While the designs of the positively- and the negatively-chirped mirrors contain around 30 layers Mo/B4C the almost unchirped mirror is a 17 layer Mo/Si/B4C stack. The mirrors have been deposited by means of Dual Ion Beam Deposition (DIBD) on flat high-polished

glass substrates. Interface losses and compound formation have been included in the calculation and could be compensated within the coating procedure.

Figs. 1.11 (a)-1.11 (c) shows the calculated reflectivity and group delay of the three multilayer mirrors versus photon energy, compared with the reflectivity measured by x-ray reflectometry using synchrotron radiation [73]. The measured and computed EUV reflectivities are in excellent agreement, revealing maximum peak reflectivities between 4 and 10 percent. Notable deviations in the peak shape appear only in Fig. 1.11 (c) near 120 eV, possibly due to minor uncertainties in the deposition layer thicknesses. In our proof-of-concept experiments, radiation at photon energies below 100 eV is suppressed by a 150 nm thick Palladium (Pd) filter (its transmittivity is shown in Fig. 1.11 (b) by the blue dash-dotted line). The throughput of this high-pass filter combination could be enhanced by fine-tuning the filter thickness and the mirrors' high-reflectivity band. Since isolated attosecond pulses can be extracted by spectral filtering from the cut-off part of the generated HH spectrum [1], the high energy extend of the spectrum must coincide with the high reflectivity range of the mirror. Reflectivity above this energy window thus does not affect the attosecond pulse generation. The three mirrors are designed to introduce substantial positive GDD, negligible GDD, and substantial negative GDD, with computed values of 19.5×10^3 as^2, -0.5×10^3 as^2, and 14×10^3 as^2, respectively.

We have implemented attosecond streaking by liberating photoelectrons from the 2p sub-shell of an ensemble of neon atoms with sub-300-attosecond EUV pulses filtered by the combination of a Pd foil and one of the band-pass multilayer mirrors described above. The energy distribution of the ejected electrons has been streaked by the controlled linearly polarized electric field of near-single-cycle near-infrared (NIR) laser pulses [68, 74, 75]. The streaked spectra for electrons collected in a narrow cone aligned with the laser polarization were recorded as a function of the delay between the ionizing EUV pulse and the streaking NIR field.

To access the temporal intensity profile of the synthesized attosecond pulses and their frequency sweep we performed a frequency-resolved optical gating (FROG) analysis [76] of the acquired streaking spectrograms. This method gives not only access to a full characterization of the laser vector potential, it allows us as well to characterize the spectral intensity distribution and the group delay variation [77, 78] of the final attosecond EUV pulse reflected from the mirrors after passing the filter, allowing for a direct comparison of its GDD with the design values of the mirrors' GDD. The resultant streaking spectrograms recorded with the three mirrors of Figs. 1.11 (a)-1.11 (c) are displayed in Figs. 1.12 (a)-1.12 (c) along with their corresponding FROG retrievals in Figs. 1.12 (d)-1.12 (f), respectively.

We can now turn our attention to a quantitative evaluation of the chirp carried by the attosecond EUV pulse in the three experiments performed with the three different mirrors. Fig. 1.13 shows the retrieved intensity and GD of the attosecond pulses after reflection off the EUV multilayer and filtering by the transmission filter as evaluated from the photo-electron spectrograms in Fig. 1.12.

The solid black lines in Figs. 1.13 (a) - 1.13 (c) show a direct measurement of the EUV pulse spectrum at the target after passing the filter and the appropriate mirror. Comparison of the retrieved EUV spectra (green dotted lines) with those directly measured photon spectra shows remarkable agreement of the bandwidth, spectral profile and central energy position. This agreement between retrieved and measured spectra highlights the precision with which EUV mirrors are designed and manufactured and demonstrates the power of attosecond streaking measurements coupled with the FROG CRAB retrieval procedure.
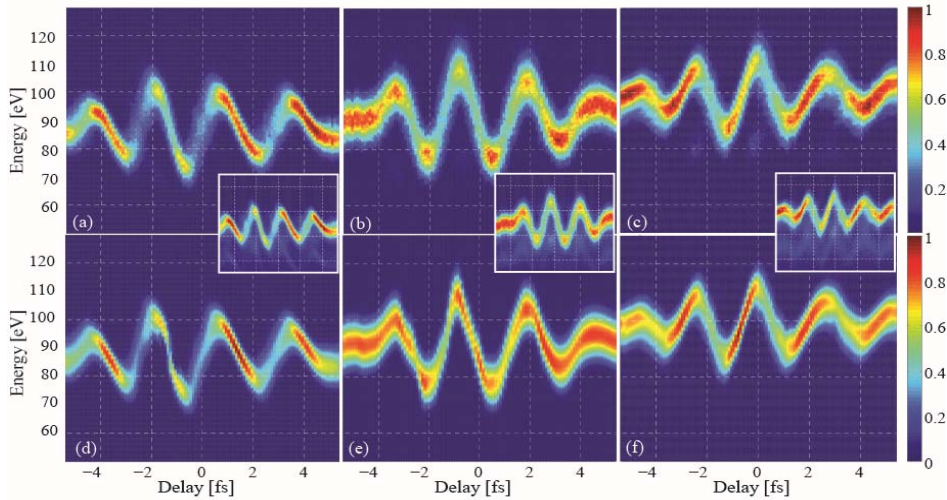

Fig. 1.12. Measured and retrieved attosecond electron streaking spectrograms, upper and lower row, respectively. Panels (a)-(c) and (d)-(f) display spectrograms recorded with attosecond pulses reflected off the mirrors described in Figs. 1.11 (a)-1.11 (c), respectively. The energy shift in the recorded spectra is proportional to the vector potential $A_L(t)$ of the streaking laser field at the instant of photoemission, hence the dependence of this energy shift on the delay between the attosecond EUV pulse and the NIR laser field reflects the temporal evolution of the NIR laser field's vector potential, $A_L(t)$. Narrowing and broadening in the streaked electron spectra at the zero crossings is displayed by enhanced and diminished electron count rates, respectively. The small insets show the energy calibrated raw data before subtraction of the background.

1.5.3.2. Chromium/Scandium Multilayer Mirror for Attosecond Pulses at 145 eV

This section will present the first application of Cr/Sc multilayer mirrors to attosecond science. The material system has been optimized for attosecond pulses and is now applied to these pulses for the first time. Most of the results have been published in [79]. The previous sections have demonstrated that multilayer mirrors provide a unique approach for beam steering, spatial and spectral shaping as well as spectral phase control with reasonably low reflective losses. It will be shown that optimizing the Cr/Sc material system is not only a key to future attosecond experiments in the water window [80], but also facilitates a promising choice for realizing new attosecond experiments at around 130-160 eV, the energy range where attosecond sources with sufficient photon flux are nowadays already available [28], but multilayer optics are very limited. Fig. 1.14 shows a

simulation comparison of certain established multilayer material systems reflecting (attosecond) HHG pulses with a central energy of 145 eV and a FWHM bandwidth of 3 eV at an angle of normal incidence of 5 degree.
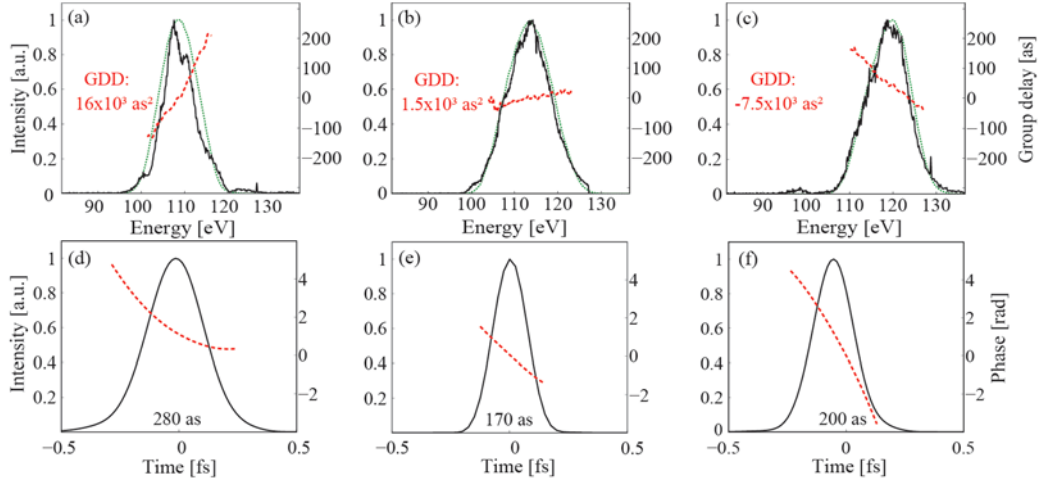

Fig. 1.13. Retrieved spectral and temporal characteristics of the attosecond EUV pulse, upper row and lower row, respectively. Panels (a), (b) and (c) display the intensity spectrum (green dotted line) and group delay (red dashed line) of the attosecond EUV pulse reflected off the mirrors described in Figs. 1.11 (a), 1.11 (b), and 1.11(c), respectively, as retrieved from the measured streaking spectrograms shown in Figs. 1.12 (a), 1.12 (b), and 1.12 (c), respectively. The black full lines depict the corresponding EUV spectra measured directly with an EUV spectrometer. The evaluated effective group-delay dispersions weighted by the final spectral EUV intensity are also shown. Panels (d), (e), (f) show the temporal intensity profile (black line) and temporal phase (red dashed line) retrieved from the streaking spectrograms of Figs. 1.12 (a), 1.12 (b), and 1.12 (c), respectively. The EUV pulse duration (full width at intensity half maximum) has been evaluated and is displayed at the bottom of each panel.
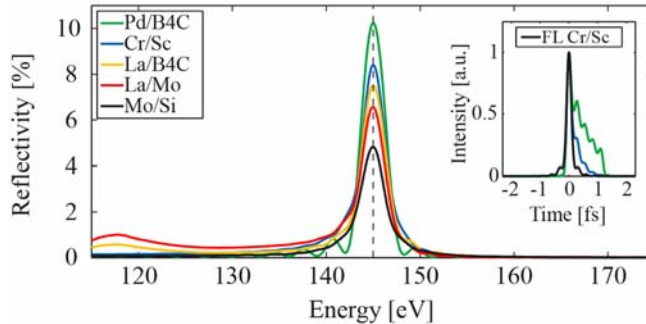

Fig. 1.14. Comparison of certain material systems at 145 eV. Simulation comparison of certain multilayer material systems for the reflection of a FWHM bandwidth of 3 eV centered at 145 eV. The small inset shows a comparison of the Cr/Sc and Pd/B4C system in the time domain including the transmission through a 200 nm thick palladium (Pd) filter. The black line shows the Fourier limit (FL) of the Cr/Sc mirror reflection.

The parameters were chosen as a trade-off between spectral and temporal resolution in high-resolution attosecond experiments. The simulations show only a weak suppression of unwanted low energy out-of band radiation in the range of ≈ 120 eV with lanthanum (La) based multilayer mirrors (La/Mo, La/B4C). The inevitable and commonly used metal filter for blocking the near-infrared (NIR) laser radiation (typically a 200 nm thick palladium (Pd) filter) cannot be used to eliminate the out-of-band radiation due to its transmission properties. As a result, chirped plateau harmonics are not sufficiently suppressed by such multilayer reflectors, which is a prerequisite for filtering isolated single attosecond pulses from the cut-off area of the high harmonic spectrum. This suppression of low energy out-of-band radiation is essential for attosecond spectroscopy experiments for e.g. delay measurements [45] or direct observation of electron propagation [34]. Well established Mo/Si mirrors, which are widely used in attosecond experiments at photon energies below the silicon L_3-edge at ≈ 100 eV, suffer from very low reflectivity above 100 eV. Other molybdenum based multilayer systems like Mo/B4C, Mo/Y, Mo/Be or Mo/Sr, which on the one hand can provide a higher degree of out-of- band radiation suppression (for Mo/B4C) accompanied with a higher reflectivity (Mo/Y, Mo/Be, Mo/Sr) [81, 82, 83, 84] but on the other hand suffer from strong spectral modulations around the main reflectivity Bragg peak by Kiessig fringes and therefore introduce additional GDD, which broadens the pulse in the time domain. Furthermore, Mo/Sr is not stable and shows long-term degradation, and beryllium is strongly toxic, thus limiting experimental adoption. A reflection comparison in the time domain of multilayer mirrors composed of Cr/Sc and a highly reflective system, here as example Pd/B4C [85], is shown in the small inset of Fig. 1.14, which already takes the transmission and the spectral phase of a 200 nm thick Pd filter into account. Whereas the pulse reflection of the Cr/Sc mirror is close to its Fourier limit and exhibits a Gaussian pulse shape, the Pd/B4C system shows unwanted temporal pulse broadening due to GDD as well as temporal modulations resulting from the multilayer reflectivity fringes. However, the Cr/Sc multilayer mirror system combines all the advantages required for applications with HHG attosecond pulses: Sufficient throughput due to the optimized reflectivity [58], suppression of out-of-band radiation components (in case of the lanthanum based systems a thicker filter can increase the suppression in the 120 eV range but reduces the overall throughput as well) and a nearly (Fourier limited) Gaussian pulse profile, both in the spectral and temporal domain.

The experimental realization of the Cr/Sc attosecond multilayer mirror was performed by dual ion-beam sputtering technique [80] together with a tailored interface polishing process [58] for a higher mirror reflectivity. For a later characterization by attosecond streaking, the mirror was also analyzed by two independent measurement techniques, hard x-ray reflectometry and EUV/soft x-ray reflectometry. Those are not shown here.

To characterize the attosecond pulses upon reflection from the Cr/Sc multilayer mirror, the well-established EUV/soft x-ray pump/NIR probe streaking technique [74] was used. Here, both the attosecond soft x-ray pulse and the NIR laser pulse are focused by a double mirror into neon gas. The soft x-ray pulse photoionizes Ne atoms, which frees photoelectrons from the 2p shell, which are then momentum-streaked by the co-propagating temporally synchronized and phase stabilized NIR laser's electric field. The

inner part of the double mirror can be moved with respect to the outer part, to introduce a temporal delay between the soft x-ray pulse, which is reflected at the mirror core, and the laser pulse, which is reflected at the outer ring. Changing the delay between the laser and the soft x-ray attosecond pulse yields a typical streaking spectrogram (Fig. 1.15 (a)).
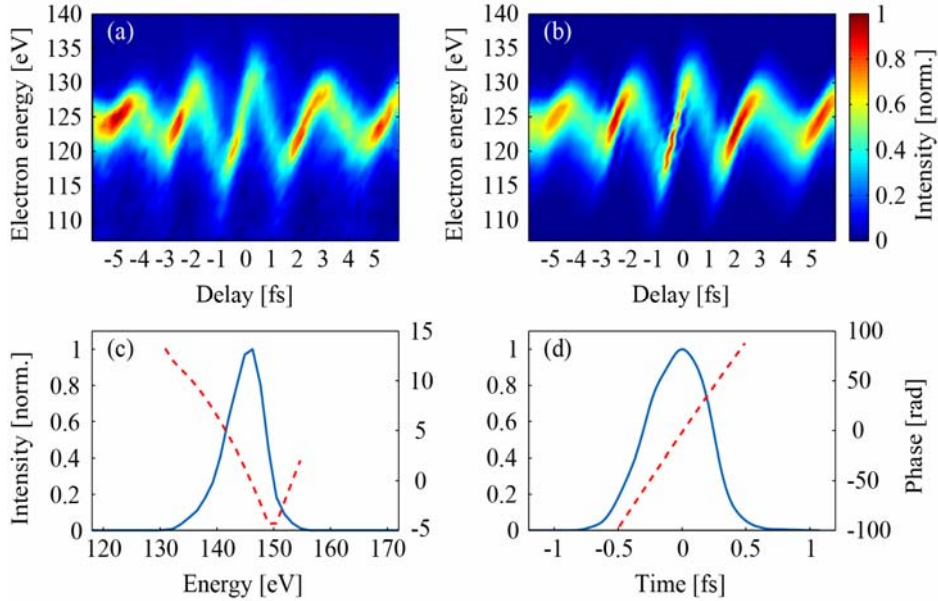

Fig. 1.15. Attosecond electron streaking at a photon energy of 145 eV. Results of an attosecond electron streaking experiment for pulse characterization in neon utilizing the Cr/Sc multilayer mirror. (a) Measured electron streaking trace and (b) the retrieved trace performed by FROG/CRAB analyses. (c) The retrieved soft x-ray pulse (solid blue) and the phase (dotted red) in the spectral domain. (d) Soft x-ray pulse and phase in the temporal domain.

FROG/CRAB [76] analysis allows for a complete reconstruction of both the intensity and the phase of the soft x-ray attosecond pulse, as well as the vector potential of the streaking laser field from a recorded spectrogram (Fig. 1.15(a)). Fig. 1.15 (b) shows the result of the appropriate FROG/CRAB retrieval as described in [78, 86]. The retrieved intensity and phase of the soft x-ray pulse are depicted in Fig. 1.15, once in the spectral (c) and once in the temporal (d) domain. Shifted by the binding energy of the Ne-2p electrons (21.6 eV) the soft x-ray pulse shows a central energy of 145.6 eV which agrees to the target and the previously described results. With the retrieved spectral bandwidth and phase being the most prominent sources of uncertainty, the temporal error can be estimated to be about 20 as. From the retrieved amplitude and phase, an attosecond pulse duration of about 580 as is found in the temporal domain which is in excellent agreement with the previous estimations (based solely on the mirror reflectivity plus the assumption of a flat mirror phase). A perfect Gaussian Fourier limited pulse with 2.9 eV bandwidth has a duration of 629 as. In summary, an optimized Cr/Sc multilayer mirror has been developed and applied for reflecting single isolated attosecond pulses at a photon energy of 145 eV with a pulse duration of 580 as.

1.5.4. Multilayer Mirrors for Attosecond Pulses in the Water Window Soft X-Ray Range

1.5.4.1. Aperiodic Multilayer Mirrors

Time resolved attosecond experiments are nowadays well established in the sub 120 eV EUV photon energy range [45, 64, 87]. With ever improving few cycle laser development toward higher pulse energies, this regime will be extended into the soft x-ray water window spectral range. Using thin filters for attosecond pulse shaping in this energy regime is limited to fixed opening and absorption edges of the used materials and thus restricts the degree of freedom. This leaves multilayer mirrors as the only key components for tailored spectral filtering and shaping of an attosecond water window pulse. For that reason, a negatively chirped aperiodic Cr/Sc multilayer mirror, optimized for reflecting sub-70 as pulses from HHG at a central photon energy of 326.3 eV (Ar L_1-edge) with a bandwidth of about 30 eV, was developed for future resonant attosecond photo ionization experiments. A positively chirped mirror was realized for comparison reasons [80].

The two different aperiodic Cr/Sc multilayer mirrors have been optimized by the thin film program *Optilayer*, a Fresnel code coupled to a needle optimization algorithm [42, 43] which is described in Section 1.3. While the first multilayer mirror has been designed for the introduction of an averaged negative chirp (the group delay dispersion is the negative second derivative of the spectral phase, GDD = -dϕ^2/dω^2) of approximately -8000 as^2 to compensate a possible positive chirp of the high harmonic plateau, a second mirror with similar parameters has been designed to introduce an averaged positive chirp of approximately +8000 as^2. Both mirrors have been designed such that their central energy coincides with the L_1-edge of Ar (326.3 eV) at an incidence angle of 45 degree. The optimized stack designs are shown in Fig. 1.16, where the negative (a) and the positive (b) design consists of around 95 individual layers.
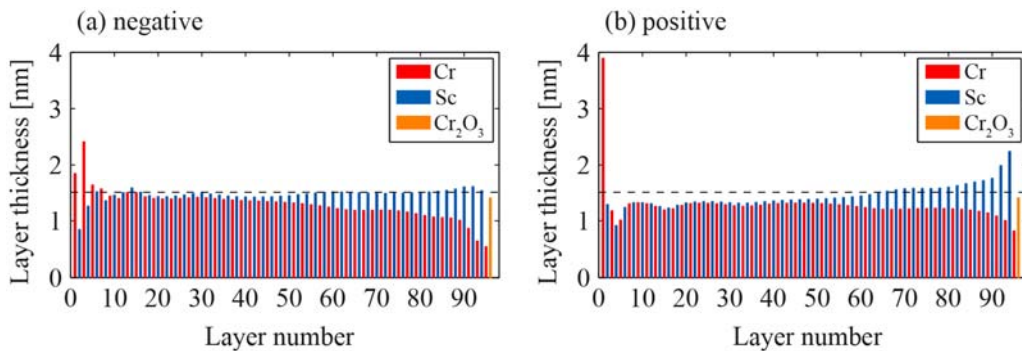

Fig. 1.16. Design of negatively and positively chirped Cr/Sc mirrors. Multilayer stack designs of the aperiodic Cr (red) and Sc (blue) layers for the introduced (a) negative, and (b) positive GDD. An arbitrary line with a layer thickness of d = 1.5 nm (dashed black) is depicted for comparison reasons.

The design has been chosen according to their robustness of GDD against small layer thickness errors. Typical layer thicknesses are between 1 nm and 2 nm, with the thinnest layers going down to 0.5 nm. For both designs a top layer of 1.4 nm Cr_2O_3 out of 0.3 nm Cr has been included in the model. These designs principally prove the large degree of freedom in customizing water window attosecond pulses both in space (substrate shape and incidence angle) and time, utilizing aperiodic Cr/Sc multilayer mirrors.

Soft x-ray reflectometry measurements were carried out at the beamline 6.3.2 of the ALS [56] to retrieve the reflectivity profile in the energy range for which the mirror designs aim at an incidence angle of 45 degree. A comparison of the simulated and measured soft x-ray reflectivity for both chirped mirrors is shown in Fig. 1.17.
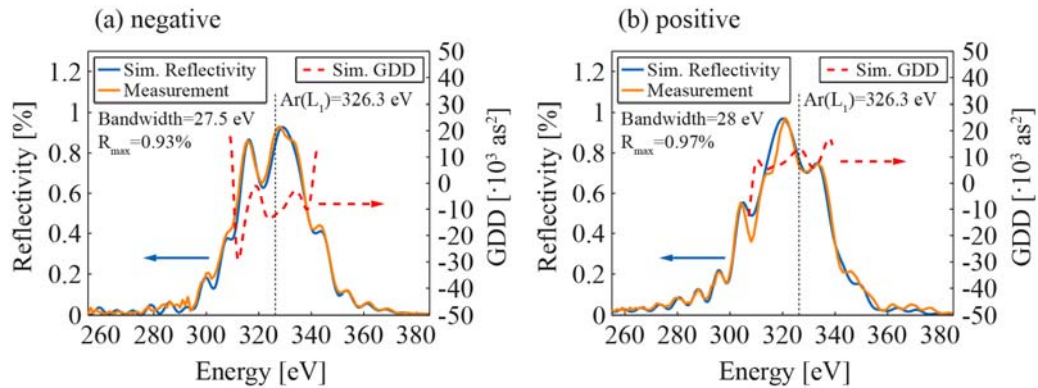

Fig. 1.17. Soft x-ray measurement of aperiodic Cr/Sc mirrors. Soft x-ray reflectivity measurement (brown) and simulation (blue) for the (a) negatively and (b) positively chirped Cr/Sc multilayer together with the corresponding simulated GDD (dashed red).

The reflectivity simulations were performed using the self-written Fresnel code of Section 1.3 and the start designs retrieved from the *Optilayer* optimization procedure [42]. An average Névot-Croce roughness factor of $\sigma = 0.49$ nm has been retrieved from simulations to account for interfacial imperfections. Both the central energy and the side peaks of the measurements and the designs coincide very well and indicate a nearly perfect experimental implementation of the simulated multilayer stack designs of Fig. 1.16. Also shown is the calculated evolution of the GDD within the reflectivity bandwidth of both multilayer systems, indicating an averaged GDD of ≈ -8000 as^2. Both multilayer systems are very similar in terms of peak energy, spectral bandwidth and peak reflectivity and only differ by the sign of their GDD. Note that the spectral multilayer phase (and thus the GDD) is not accessible by simple reflectivity measurements. Measurements of the spectral phase, by soft x-ray reflectometry, have been reported by detecting the standing-wave assisted total electron yield from the multilayer surface as a function of the photon energy around the Bragg peak [88, 89]. While this method is very suitable for periodic multilayer systems, its accuracy is limited when applied to aperiodic systems with a weak standing wave. On the other hand, one can characterize the spectral phase with two attosecond methods, the RABBITT-technique [63, 90] or by attosecond photoelectron streaking

spectroscopy providing access to a full characterization of the reflected attosecond pulse both in amplitude and phase [68, 72]. However, for the water window the implementation of both attosecond techniques has not been established yet due to a lack of sufficient photon flux from HHG attosecond sources in this spectral range. Here we analyze and estimate the influence of the layer errors on the reflectivity and the GDD via simulations. The rather perfect match of the designed and the measured reflectivity in Fig. 1.17 proofs the correct elimination of systematic deposition errors and leaves only random errors to be analyzed. Both the simulated reflectivity and the GDD of the original design of the negatively chirped multilayer is compared to slightly modified designs. The designs have been chosen randomly by joggling each layer thickness within predefined limits and the merit function (MF) of the reflectivity, as well as the corresponding averaged GDD value, was calculated to analyze the quality of reflectivity and GDD simulations:

$$MF = \sqrt{\frac{1}{N}\sum_{i=1}^{N}\left(R_{(sim),i} - R_{(softx-ray),i}\right)^2} ,$$
(1.31)

where N is the total number of wavelength sampling with an integer i representing the position of the sampling equally spaced. 100 designs have been averaged per allowed error and both the reflectivity and the GDD deviations have been calculated. Designs with an overall stack height deviation of more than 0.8 % have been left out due to discrepancy with profilometry investigations. From Fig. 1.18(a) it can be deduced, that the average random thickness error is less than 0.5 %, corresponding to an average layer thickness error of approximately 0.05 angstrom.
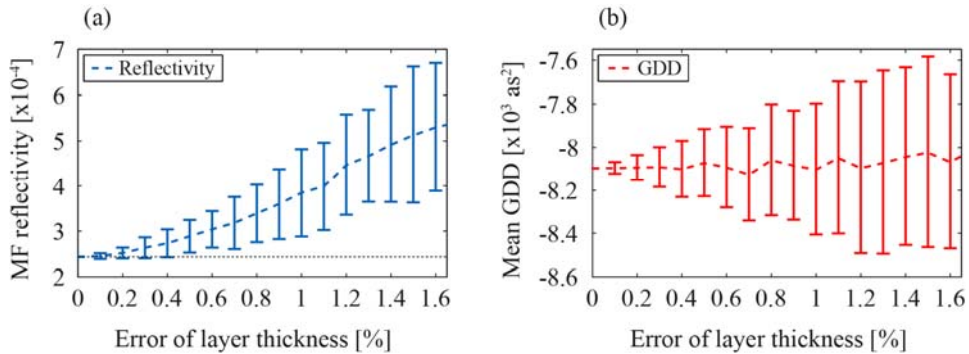

Fig. 1.18. Merit function and GDD dependence on layer thickness errors. (a) Merit function for the simulated reflectivity and the soft x-ray measurement for different layer thickness errors. (b) Mean GDD for different layer errors.

Fig. 1.18(b) shows, that the GDD mean value stays nearly constant independent of the layer errors. The upper limit of the layer errors of 0.5 % corresponds to a maximum mean GDD error of approximately ± 150 as^2. To summarize the results, we have a standard deviation of ≈ 0.024 % in the soft x-ray reflectivity and a mean GDD of -8090 $\pm$ 150 as^2 for the aperiodic negatively chirped Cr/Sc multilayer mirror.

1.6. Metrology and Application

This section will describe three different measurement, characterization and application techniques which are used in attosecond science. The techniques allow for the access to attosecond phenomena in matter and utilize the attosecond pulses being reflected off and shaped by attosecond multilayer mirrors, described in the previous sections. Multilayer mirrors for attosecond pulses are therefore the key components in those experiments gaining deep physical insight into the dynamics of matter. This paves the way toward eventually controlling chemical or biological processes in the future.

1.6.1. Streaking Measurements

The last step after the generation and shaping of attosecond pulses is their measurement and characterization. Indirect measurement techniques must be used as no electronics are fast enough to map their temporal structure. One way for the pulse characterization is to cross-correlate the photoemission of the EUV/soft x-ray pulse (pump) with the electric field of the driving laser (probe). The driving laser pulse is used as a probe, since it is intrinsically synchronized with the EUV pulse by the HHG process. This cross-correlation results in a time delay dependent spectral photoelectron trace which can be used to reconstruct both pulses. This method is called attosecond streak camera or atomic transient recorder [74]. Both the EUV and laser beam are focused into an interaction medium (gas, solid, liquid) where the EUV ionizes the atoms. The ionized electrons are freed and inherit all the characteristics of the attosecond pulse regarding energy, pulse duration and phase nevertheless with a shifted kinetic energy, i.e. reduced by the binding energy W_b of the original electron level (e.g. 21.6 eV for the Ne 2p electrons):

$$W_{kin}\left(t_0\right)=\hbar\omega-W_b. \tag{1.32}$$

After the ionization, the electrons are accelerated by the electric field E(t) of the laser resulting in a time dependent momentum:

$$p(t)=p\left(t_0\right)-e\int_{t_0}^{t} E\left(\tau\right)d\tau=p\left(t_0\right)-eA\left(t_0\right)+eA\left(t\right), \tag{1.33}$$

where t_0 is the time of ionization, A the vector potential and p(t$_0$) = sqrt(2mW$_{kin}$(t$_0$)) the instant momentum. After the laser has passed, the electron's final momentum is only dependent on the vector potential at the time of its ionization, since A(t=∞) = 0 when the laser is no longer present at t = ∞:

$$p\left(\infty\right)=p\left(t_0\right)-eA\left(t_0\right). \tag{1.34}$$

Measuring the electron spectrum for different time delays between the laser and the attosecond pulse results in a streaking trace like shown in Fig. 1.15. This spectrogram allows for a complete retrieval of both the vector potential of the laser and the characteristic of the attosecond pulse by FROG/CRAB [76, 78, 86, 91]. The analysis

reveals the intensity as well as nonlinear phase terms (e.g. a possible chirp) of the attosecond pulse thus a complete reconstruction of the temporal structure. Summarized, attosecond streaking is sensitive not only to the EUV spectrum, but also to its phase which allows fully characterizing the EUV pulse. As the vector potential of the laser pulse is measured as well, it can also be completely characterized.

1.6.2. Transient Absorption Measurements

Attosecond transient absorption spectroscopy (ATAS) is an extension of absorption spectroscopy. Ultrafast transient absorption spectroscopy, an example of non-linear spectroscopy, measures changes in the absorbance/transmittance in a sample. The sample is excited by a pump pulse (UV–NIR) and the corresponding change in transmittance is probed by an ultrafast attosecond pulse as a function of the temporal delay of both pulses [92]. By means of highly intense few-cycle infrared pulses one modifies for example the electrical conductivity of a dielectric. The strong electric field of the laser changes the population of the conduction band and transfers the dielectric from an insulator to a conductor [93]. The population of the valence and conduction band influences the photoemission of the core states and changes consequently the absorption property of the material in the EUV range at element-specific absorption edges. This measurement technique enabled for the first time the observation of the motion of a superposition of valence electrons in krypton in real time on the attosecond timescale [32]. Applying this pump-probe method e.g. to semiconductors, electron-hole pairs are generated by the laser pulse and the occupancy of connected valence and conduction bands states is probed by the attosecond EUV pulse. The desired electron-hole pair density can be generated by tuning the laser intensity. The underlying dynamics are imprinted in the probing EUV absorption spectrum, since the absorption of the EUV photon is sensitive to the conduction band population via the interaction of the EUV excited electron with electrons injected by the pump pulse. Introducing a controlled time delay between the probe and pump pulse reveals information about the filling/emptying rate of the states by the probe [94]. This ensures a fundamental insight into the predominant carrier dynamics.

1.6.3. The RABBITT Technique

A second technique for the characterization of attosecond pulses is usually referred to as RABBITT (Reconstruction of Attosecond harmonic Beating By Interference of Two-photon Transitions) [63, 90]. It is known that HHG occurs when an intense laser pulse is focused into a gas target. If the focused IR laser pulse consists now of several cycles, in contrast to close to single cycle in Section 1.6.1 (e.g. $\Delta\tau = 30$ fs versus $\Delta\tau = 5$ fs), the emitted harmonics will also be confined in short attosecond pulses, which are continuously generated every half cycle of the IR pulse, but now resulting in an attosecond pulse train (APT) with a strongly modulated EUV spectrum. The number of electric field cycles increases with longer pulses, i.e. more attosecond pulses are generated. The interference of a higher number of pulses is responsible for the strongly modulated spectrum in contrast to a superimposed plateau spectrum for the case of few cycle driver pulses. These APTs can be characterized by RABBITT. Spectrally and temporally filtered

EUV-APTs are focused into a noble gas which gets ionized. The freed electrons exhibit kinetic energies which reflect the corresponding high harmonic photon energies (separated by $2\omega_0$). Sidebands peaks will appear in the electron energy spectrum if a moderately intense IR field is also focused into the noble gas. These sidebands are based on two-photon two-color ionization by one EUV photon and one infrared laser photon. Varying the time delay between the EUV and the IR modulates the sideband signal which originates from the interference between two processes: absorption of an EUV photon and an IR photon ($q\omega_{IR}+\omega_{IR}$), and absorption of an EUV photon and emission of an IR photon ($(q+2)\omega_{IR}-\omega_{IR}$) [63]. As the width and especially the relative temporal position of a sideband maximum is determined by the phase difference between two neighboring fundamental harmonic peaks, only the oscillation of the high harmonic ionization signal in the delay dependent electron energy spectrum contains the exact spectral phase information of the EUV pulses. This allows a precise characterization of the attosecond pulse trains by RABBITT. However, the RABBITT technique will probably be limited to the lower attosecond energy regime as few cycle laser pulses, exhibiting a high electric field amplitude, are needed to push attosecond science to higher photon energies (e.g. the water window) in the near future.

1.7. Outlook

Big achievements have already been made in terms of the performance of multilayer mirrors for attosecond pulses, but further optimization and application are possible. The realization of the first chirped multilayer mirrors for the visible spectral energy range and their first proof of successful femtosecond pulse compression was the key to implement the idea behind those mirrors in today's high-power laser systems and to make them to working horses in laser technology, since chirped laser amplification would be impossible without such mirrors. The realization of chirped mirrors for attosecond pulses in the EUV and even soft x-ray energy range was possible by fully controlling atomic layer-by-atomic layer deposition and may also open doors to key technologies and new exciting experiments like the mirrors for the visible range already do today.

1.7.1. The Way Toward Ever Shorter Pulses - Approaching the Atomic Unit of Time

The cornerstone of attosecond physics was the key for ever shorter pulses, since the ultrafast femtosecond pulses were superseded after several decades by attosecond pulses. The first experiment for the generation of isolated pulses has proven a temporal duration of 650 attoseconds [1] and lots of subsequent experiments have realized even shorter pulses, resulting in the nowadays shortest flashes of light below 100 attosecond, isolated attosecond pulses with a temporal duration of 67 attoseconds [95] and 80 attoseconds [68].

With the investigation of ever more intense laser systems (HHG cutoff energy: ~Intensity) and in parallel going toward laser systems with longer wavelengths (HHG cutoff energy: $\sim\lambda^2$) an ever higher cutoff energy, up to the keV, is achieved [96] and as a consequence broader spectra are accessible and therefore shorter pulses can in principle be achieved. A time scale often aimed and given is the time it takes an electron to complete one rad of its

orbit in the ground state of hydrogen [97]: $\tau_{atomic} = \hbar/2U_H \approx 24$ as (often called the atomic unit of time), where U_H is the binding energy of the hydrogen atom (13.6 eV). The key is multicolor high-peak-power excitation in the HHG process [98]. So, the HHG field is aiming toward high-energy few-cycle femtosecond mid-IR lasers as prospective driver sources for strong-field applications, offering a high photon flux in a broad energy window and the opportunity for ever shorter time resolutions, approaching the atomic unit of time. Very recently the first accuracy below the attosecond time scale was achieved. Scientists succeeded in determine the photoemission time in helium with an accuracy of 0.85 attoseconds or 850 zeptoseconds [99].

1.7.2. Multilayer Mirrors for HHG Photon Energies up to the keV Spectral Range

The previous section described the way toward ever higher photon energies in HHG but neglected one important parameter: the high photon number needed for low-cross-section attosecond experiments. Consequently, the sources should offer a high photon number $>10^{10}$ in the soft x-ray range and multilayer mirrors, being used for beam guiding, beam shaping or beam focusing, should ensure a high photon throughput for high attosecond pulse intensities in the target to be investigated. The way toward higher photon energies combined with a high photon flux leaves only one way open for multilayer mirrors: toward grazing incidence optics. Grazing incidence optics are the key for photon energies above the water window (> 543.1 eV= oxygen 1s) up to the keV due to four distinct reasons:

- Eq. (1.16) demonstrates a high single interface reflectivity for grazing incidence.

- The Bragg Eq. (1.20) shows the necessity for grazing optics in case of the keV: A photon energy of 1000 eV corresponds to a wavelength of $\lambda = 1.2398$ nm, which leads in case of normal incidence to a $\lambda/2$ period in a multilayer mirror. Assuming a typical two material systems one ends up in a layer thickness of ~ 0.3 nm, which is close to the limit of technical realization.

- The roughness Eq. (1.28) demonstrates how one can minimize the influence of the roughness on the reflectivity performance: The lower the σ/d-ratio the lower is the reflectivity loss. One thus can minimize the reflectivity loss by reducing the interface roughness σ or increase the period thickness d. Keeping the center energy from a multilayer mirror constant leads in case of a higher period thickness to a lower grazing incidence angle. This overlaps with the previous reason. Typical roughness values are in the range of 0.4-0.6 nm, so comparable thickness values are strongly not recommended.

- The bandwidth Eq. (1.22) shows the advantage for attosecond pulses. In case of grazing incidence only few layers can contribute to the overall reflectivity which results at a certain energy in a higher bandwidth support. According to Eq. (1.23) this offers the opportunity for shorter pulses.

1.8. Conclusions

Multilayer mirrors investigations over the last decades paved their application way from the visible/infrared to the EUV/soft x-ray spectral range in terms of spectral characteristic and from the picosecond/femtosecond down to the attosecond regime in terms of temporal consideration. Those mirrors are nowadays already used by default in attosecond science in the EUV range, thanks to the big improvements being realized by an optimized combination of deposition, simulation and characterization methods. Due to their high degree of freedom multilayer mirrors will remain a keycomponent in attosecond beamlines as pulse shaping element and further investigations will open the way toward attosecond physics at ever higher spectral ranges and with ever shorter pulses.

Acknowledgements

References

[1]. M. Hentschel, R. Kienberger, Ch. Spielmann, G. A. Reider, N. Milosevic, T. Brabec, P. Corkum, U. Heinzmann, M. Drescher, F. Krausz, Attosecond metrology, *Nature*, Vol. 414, 2001, pp. 509-513.

[2]. C. Morawe, M. Osterhoff, Hard x-ray focusing with curved reflective multilayers, *X-Ray Optics and Instrumentation*, Vol. 2010, 2010, pp. 1-8.

[3]. J. Schmidt, A. Guggenmos, M. Hofstetter, S. H. Chew, U. Kleineberg, Generation of circularly polarized high harmonic radiation using a transmission multilayer quarter waveplate, *Optics Express*, Vol. 23, 2015, pp. 33564-33578.

[4]. M. Zürch, J. Rothhardt, S. Hädrich, S. Demmler, M. Krebs, J. Limpert, A. Tünnermann, A. Guggenmos, U. Kleineberg, C. Spielmann, Real-time and sub-wavelength ultrafast coherent diffraction imaging in the extreme ultraviolet, *Scientific Reports*, Vol. 4, 2014, 7356.

[5]. E. Spiller, Reflective multilayer coatings for the far UV region, *Applied Optics,* Vol. 15, 1976, pp. 2333-2338.

[6]. S. Bajt, J. B. Alameda, J. Barbee, W. Troy, W. M. Clift, J. A. Folta, B. Kaufmann, E. A. Spiller, Improved reflectance and stability of Mo-Si multilayers, *Optical Engineering,* Vol. 41, 2002, pp. 1797-1804.

[7]. I. V. Kozhevnikov, L. L. Balakireva, A. I. Fedorenko, I. A. Kopealets, V. E. Levashov, A. N. Stetsenko, I. I. Struk, A. V. Vinogradov, Synthesis and measurement of Os-Si multilayer mirrors optimized for the wavelength 380 Å, *Optics Communications*, Vol. 125, 1996,
pp. 13-17.

[8]. S. Rajesh, V. Arivazhagan, M. M. Parvathi, Structural, optical and electrical properties of vacuum evaporated PbSe/ZnSe multilayer thin films, *AIP Conference Proceedings*, Vol. 1451, 2012, pp. 197-199.

[9]. K. M. Skulina, C. S. Alford, R. M. Bionta, D. M. Makowiecki, E. M. Gullikson, R. Soufli, J. B. Kortright, J. H. Underwood, Molybdenum/beryllium multilayer mirrors for normal incidence in the extreme ultraviolet, *Applied Optics*, Vol. 34, 1995, pp. 3727-3730.

[10]. S. Bajt, D. G. Stearns, P. A. Kearney, Investigation of the amorphousto-crystalline transition in Mo/Si multilayers, *Journal of Applied Physics*, Vol. 90, 2001, pp. 1017-1025.

[11]. P. N. Rao, M. Nayak, G. S. Lodha, S. K. Rai, A. K. Srivastava, M. H. Modi, A. Sagdeo, Fabrication and evaluation of large area Mo/Si soft x-ray multilayer mirrors at Indus SR facilities, *Advances in Optical Technologies*, Vol. 2012, 2012, pp. 1-8.

[12]. D. L. Voronov, P. Gawlitza, R. Cambie, S. Dhuey, E. M. Gullikson, T. Warwick, S. Braun, V. V. Yashchuk, H. A. Padmore, Conformal growth of Mo/Si multilayers on grating substrates using collimated ion beam sputtering, *Journal of Applied Physics*, Vol. 111, 2012, 093521.

[13]. A. El Hajj, B. Lucas, M. Chakaroun, R. Antony, B. Ratier, M. Aldissi, Optimization of ZnO/Ag/ZnO multilayer electrodes obtained by Ion Beam Sputtering for optoelectronic devices, *Thin Solid Films*, Vol. 520, 2012, pp. 4666-4668.

[14]. M. Grigonis, É. J. Knystautas, C/Si multilayer mirrors for the 25–30-nm wavelength region, *Applied Optics*, Vol. 36, 1997, pp. 2839-2842.

[15]. Z. Wang, H. Zhao, Q. Yao, J. Xu, H. Kimura, Structure and magnetism of ZnO/Co multilayers prepared by pulsed laser deposition, *Crystal Research and Technology*, Vol. 47, 2012, pp. 799-803.

[16]. K. Siraj, M. Khaleeq-ur Rahman, M. S. Rafique, M. Z. Munawar, S. Naseem, S. Riaz, Pulsed laser deposition and characterization of multilayer metalcarbon thin films, *Applied Surface Science*, Vol. 257, 2011, pp. 6445-6450.

[17]. D. B. Chrisey, G. K. Hubler, Pulsed Laser Deposition of Thin Films, *Wiley*, 1994.

[18]. D. Martínez-Galarce, R. Soufli, D. L. Windt, M. Bruner, E. Gullikson, S. Khatri, E. Spiller, J. C. Robinson, S. Baker, E. Prast, Multisegmented, multilayer-coated mirrors for the solar ultraviolet imager, *Optical Engineering*, Vol. 52, 2013, 095102.

[19]. C. Wagner, N. Harned, EUV lithography: Lithography gets extreme, *Nature Photonics,* Vol. 4, 2010, pp. 24-26.

[20]. W. Chao, J. Kim, S. Rekawa, P. Fischer, E. H. Anderson, Demonstration of 12 nm resolution fresnel zone plate lens based soft x-ray microscopy, *Optics Express,* Vol. 17, 2009, pp. 17669-17677.

[21]. J.-Ph. Champeaux, Ph. Troussel, B. Villier, V. Vidal, T. Khachroum, B. Vidal, M. Krumrey, Development and realization of non-periodic W/Si multilayer mirrors for 5–14 keV x-ray plasma diagnostic, *Nuclear Instruments and Methods in Physics Research Section A*, Vol. 581, 2007, pp. 687-694.

[22]. N. V. Andronova, V. G. Kohn, A. I. Chechin, Multilayer mirrors as synchrotron radiation monochromators, *Nuclear Instruments and Methods in Physics Research Section A*, Vol. 359, 1995, pp. 131-134.

[23]. M. Ferray, A. L'Huillier, X. F. Li, L. A. Lompre, G. Mainfray, C. Manus, Multiple-harmonic conversion of 1064 nm radiation in rare gases, *Journal of Physics B: Atomic, Molecular and Optical Physics*, Vol. 21, 1988, pp. L31-L35.

[24]. M. Prasciolu, A. F. G. Leontowich, K. R. Beyerlein, S. Bajt, Thermal stability studies of short period Sc/Cr and Sc/B4C/Cr multilayers, *Applied Optics*, Vol. 53, 2014, pp. 2126-2135.

[25]. W. Helml, A. R. Maier, W. Schweinberger, I. Grguras, P. Radcliff, G. Doumy, C. Roedig, J. Gagnon, M. Messerschmidt, S. Schorb, C. Bostedt, F. Grüner, L. F. DiMauro, D. Cubaynes, J. D. Bozek, T. Tschentscher, J. T. Costello, M. Meyer, R. Coffee, S. Düsterer, A. L. Cavalieri,

R. Kienberger, Measuring the temporal structure of few-femtosecond free-electron laser x-ray pulses directly in the time domain, *Nature Photonics*, Vol. 8, 2014, pp. 950-957.

[26]. M. F. Kling, M. J. J. Vrakking, Attosecond electron dynamics, *Annual Review of Physical Chemistry*, Vol. 59, 2008, pp. 463-492.

[27]. M. Fieß, M. Schultze, E. Goulielmakis, B. Dennhardt, J. Gagnon, M. Hofstetter, R. Kienberger, F. Krausz, Versatile apparatus for attosecond metrology and spectroscopy, *Review of Scientific Instruments*, Vol. 81, 2010, 093103.

[28]. W. Schweinberger, A. Sommer, E. Bothschafter, J. Li, F. Krausz, R. Kienberger, M. Schultze, Waveform-controlled near-single-cycle milli-joule laser pulses generate sub-10 nm extreme ultraviolet continua, *Optics Letters*, Vol. 37, 2012, pp. 3573-3575.

[29]. P. Corkum, Plasma perspective on strong-field multiphoton ionization, *Physical Review Letters*, Vol. 71, 1993, pp. 1994-1997.

[30]. D. Descamps, C. Lyngå, J. Norin, A. L'Huillier, C.-G. Wahlström, J.-F. Hergott, H. Merdji, P. Salières, M. Bellini, T. W. Hänsch, Extreme ultraviolet interferometry measurements with high-order harmonics, *Optics Letters*, Vol. 25, 2000, pp. 135-137.

[31]. J. Lee, D. R. Carlson, R. J. Jones, Optimizing intracavity high harmonic generation for XUV fs frequency combs, *Optics Express*, Vol. 19, 2011, pp. 23315-23326.

[32]. E. Goulielmakis, Z.-H. Loh, A. Wirth, R. Santra, N. Rohringer, V. S. Yakovlev, S. Zherebtsov, T. Pfeifer, A. M. Azzeer, M. F. Kling, S. R. Leone, F. Krausz, Real-time observation of valence electron motion, *Nature*, Vol. 466, 2010, pp. 739-743.

[33]. M. Nisoli, P. Decleva, F. Calegari, A. Palacios, F. Martín, Attosecond electron dynamics in molecules, *Chemical Review*, 2017, pp. 10760-10825.

[34]. S. Neppl, R. Ernstorfer, A. L. Cavalieri, C. Lemell, G. Wachter, E. Magerl, E. M. Bothschafter, M. Jobst, M. Hofstetter, U. Kleineberg, J. V. Barth, D. Menzel, J. Burgdörfer, P. Feulner, F. Krausz, R. Kienberger, Direct observation of electron propagation and dielectric screening on the atomic length scale, *Nature*, Vol. 517, 2015, pp. 342-346.

[35]. S. H. Chew, F. Süßmann, C. Späth, A. Wirth, J. Schmidt, S. Zherebtsov, A. Guggenmos, A. Oelsner, N. Weber, J. Kapaldo, A. Gliserin, M. I. Stockman, M. F. Kling, U. Kleineberg, Time-of-flight-photoelectron emission microscopy on plasmonic structures using attosecond extreme ultraviolet pulses, *Applied Physics Letters*, Vol. 100, 2012, 051904.

[36]. Z. Tao, C. Chen, T. Szilvasi, M. Keller, M. Mavrikakis, H. Kapteyn, M. Murnane, Direct time-domain observation of attosecond final-state lifetimes in photoemission from solids, *Science*, Vol. 353, 2016, pp. 62-67.

[37]. D. Attwood, Soft X-Rays and Extreme Ultraviolet Radiation: Principles and Applications, *Cambridge University Press*, 2007.

[38]. B. L. Henke, E. M. Gullikson, J. C. Davis, X-ray interactions: photoabsorption, scattering, transmission, and reflection at E=50-30000 eV, Z=1-92, *Atomic Data and Nuclear Data Tables,* Vol. 54, 1993, pp. 181-342.

[39]. E. Spiller, Soft X-Ray Optics, *SPIE Optical Engineering Press*, 1994.

[40]. M. Trubetskov, A. Tikhonravov, V. Pervak, Time-domain approach for designing dispersive mirrors based on the needle optimization technique. Theory, *Optics Express*, Vol. 16, 2008, pp. 20637-20647.

[41]. V. Pervak, A. V. Tikhonravov, M. K. Trubetskov, S. Naumov, F. Krausz, A. Apolonski, 1.5-octave chirped mirror for pulse compression down to sub-3 fs, *Applied Physics B*, Vol. 87, 2006, pp. 5-12.

[42]. A. V. Tikhonravov, M. K. Trubetskov, G. W. DeBell, Optical coating design approaches based on the needle optimization technique, *Applied Optics*, Vol. 46, 2007, pp. 704-710.

[43]. V. Yakovlev, G. Tempea, Optimization of chirped mirrors, *Applied Optics,* Vol. 41, 2002, pp. 6514-6520.

[44]. V. Pervak, C. Teisset, A. Sugita, S. Naumov, F. Krausz, A. Apolonski, High-dispersive mirrors for femtosecond lasers, *Optics Express,* Vol. 16, 2008, pp. 10220-10233.

[45]. M. Schultze, M. Fieß, N. Karpowicz, J. Gagnon, M. Korbman, M. Hofstetter, S. Neppl, A. L. Cavalieri, Y. Komninos, T. Mercouris, C. A. Nicolaides, R. Pazourek, S. Nagele, J. Feist, J. Burgdörfer, A. M. Azzeer, R. Ernstorfer, R. Kienberger, U. Kleineberg, E. Goulielmakis, F. Krausz, V. S. Yakovlev, Delay in photoemission, *Science*, Vol. 328, 2010, pp. 1658-1662.

[46]. J. H. Underwood, T. W. Barbee, Layered synthetic microstructures as Bragg diffractors for x-rays and extreme ultraviolet: theory and predicted performance, *Applied Optics*, Vol. 20, 1981, pp. 3027-3034.

[47]. L. G. Parratt, Surface studies of solids by total reflection of x-rays, *Physical Review*, Vol. 95, 1954, pp. 359-369.

[48]. A. L. Aquila, F. Salmassi, F. Dollar, Y. Liu, E. Gullikson, Developments in realistic design for aperiodic Mo/Si multilayer mirrors, *Optics Express*, Vol. 14, 2006, pp. 10073-10078.

[49]. U. Kleineberg, H.-J. Stock, A. Kloidt, B. Schmiedeskamp, U. Heinzmann, S. Hopfe, R. Scholz, Interface stability and silicide formation in high temperature stable MoxSi1-x/Si multilayer soft x-ray mirrors studied by means of x-ray diffraction and HRTEM, *Physica Status Solidi (A)*, Vol. 145, 1994, pp. 539-550.

[50]. P. Debye, Interferenz von röntgenstrahlen und wärmebewegung, *Annalen der Physik*, Vol. 348, 1913, pp. 49-92.

[51]. I. Waller, Zur frage der einwirkung der wärmebewegung auf die interferenz von röntgenstrahlen, *Zeitschrift für Physik*, Vol. 17, 1923, pp. 398-408.

[52]. L. Névot, P. Croce, Caractérisation des surfaces par réflexion rasante de rayons x. Application à l'étude du polissage de quelques verres silicates, *Revue de Physique Appliquee*, Vol. 15, 1980, pp. 761-779.

[53]. E. Chi, J. Shim, J. Kwak, H. Baik, Silicide formation by solid-state diffusion in MO/Si multilayer thin films, *Journal of Materials Science*, Vol. 31, 1996, pp. 3567-3572.

[54]. M. Hofstetter, A. Aquila, M. Schultze, A. Guggenmos, S. Yang, E. Gullikson, M. Huth, B. Nickel, J. Gagnon, V. S. Yakovlev, E. Goulielmakis, F. Krausz, U. Kleineberg, Lanthanum–molybdenum multilayer mirrors for attosecond pulses between 80 and 130 eV, *New Journal of Physics*, Vol. 13, 2011, 063038.

[55]. E. Gerald, J. Jellison, Data Analysis for Spectroscopic Ellipsometry, in Handbook of Ellipsometry, (F. A. Jenkins, H. E. White, Ed.), *William Andrew Publishing*, 2005, pp. 237-296.

[56]. E. M. Gullikson, S. Mrowka, B. B. Kaufmann, Recent developments in EUV reflectometry at the advanced light source, *Emerging Lithographic Technologies V, Proceedings of SPIE*, Vol. 4343, 2001, pp. 363-373.

[57]. S. Singh, S. Basu, P. Bhatt, A. K. Poswal, Kinetics of alloy formation at the interfaces in a Ni-Ti multilayer: x-ray and neutron reflectometry study, *Physical Review B*, Vol. 79, 2009, 195435.

[58]. A. Guggenmos, S. Radünz, R. Rauhut, M. Hofstetter, S. Venkatesan, A. Wochnik, E. M. Gullikson, S. Fischer, B. Nickel, C. Scheu, U. Kleineberg, Ion polished Cr/Sc attosecond multilayer mirrors for high water window reflectivity, *Optics Express*, Vol. 22, 2014, pp. 26526-26536.

[59]. F. Hamelmann, G. Haindl, J. Schmalhorst, A. Aschentrup, E. Majkova, U. Kleineberg, U. Heinzmann, A. Klipp, P. Jutzi, A. Anopchenko, M. Jergel, S. Luby, Metal oxide/silicon oxide multilayer with smooth interfaces produced by in situ controlled plasma-enhanced MOCVD, *Thin Solid Films*, Vol. 358, 2000, pp. 90-93.

[60]. R. L. Thornton, R. D. Burnham, W. Streifer, High reflectivity GaAs-AlGaAs mirrors fabricated by metalorganic chemical vapor deposition, *Applied Physics Letters*, Vol. 45, 1984, pp. 1028-1030.

[61]. P. B. Corkum, F. Krausz, Attosecond science, *Nature Physics*, Vol. 3, 2007, pp. 381-387.

[62]. F. Krausz, M. Ivanov, Attosecond physics, *Review of Modern Physics*, Vol. 81, 2009, pp. 163-234.

[63]. R. López-Martens, K. Varjú, P. Johnsson, J. Mauritsson, Y. Mairesse, P. Salières, M. B. Gaarde, K. J. Schafer, A. Persson, S. Svanberg, C.-G. Wahlström, A. L'Huillier, Amplitude and phase control of attosecond light pulses, *Physical Review Letters*, Vol. 94, 2005, 033001.

[64]. G. Sansone, E. Benedetti, F. Calegari, C. Vozzi, L. Avaldi, R. Flammini, L. Poletto, P. Villoresi, C. Altucci, R. Velotta, S. Stagira, S. De Silvestri, M. Nisoli, Isolated single-cycle attosecond pulses, *Science*, Vol. 314, 2006, pp. 443-446.

[65]. T. Rohwer, S. Hellmann, M. Wiesenmayer, C. Sohrt, A. Stange, B. Slomski, A. Carr, Y. Liu, L. M. Avila, M. Kallane, S. Mathias, L. Kipp, K. Rossnagel, M. Bauer, Collapse of long-range charge order tracked by time-resolved photoemission at high momenta, *Nature*, Vol. 471, 2011, pp. 490-493.

[66]. A.-S. Morlens, R. López-Martens, O. Boyko, P. Zeitoun, P. Balcou, K. Varjú, E. Gustafsson, T. Remetter, A. L'Huillier, S. Kazamias, J. Gautier, F. Delmotte, M.-F. Ravet, Design and characterization of extreme-ultraviolet broadband mirrors for attosecond science, *Optics Letters*, Vol. 31, 2006, pp. 1558-1560.

[67]. Y. A. Uspenskii, V. E. Levashov, A. V. Vinogradov, A. I. Fedorenko, V. V. Kondratenko, Y. P. Pershin, E. N. Zubarev, S. Mrowka, F. Schäfers, Sc-Si normal incidence mirrors for a VUV interval of 35-50 nm, *Nuclear Instruments and Methods in Physics Research Section A*, Vol. 448, 2000, pp. 147-151.

[68]. E. Goulielmakis, M. Schultze, M. Hofstetter, V. S. Yakovlev, J. Gagnon, M. Uiberacker, A. L. Aquila, E. M. Gullikson, D. T. Attwood, R. Kienberger, F. Krausz, U. Kleineberg, Single-cycle nonlinear optics, *Science*, Vol. 320, 2008, pp. 1614-1617.

[69]. A. Guggenmos, A. Akil, M. Ossiander, M. Schäffer, A. M. Azzeer, G. Boehm, M.-C. Amann, R. Kienberger, M. Schultze, U. Kleineberg, Attosecond photoelectron streaking with enhanced energy resolution for small-bandgap materials, *Optics Letters*, Vol. 41, 2016, pp. 3714-3717.

[70]. C. Bourassin-Bouchet, S. de Rossi, F. Delmotte, Multilayer Mirrors for Coherent Extreme-Ultraviolet and Soft X-ray Sources, in Optical Technologies for Extreme-Ultraviolet and Soft X-ray Coherent Sources (F. Canova, L. Poletto, Ed.), Springer Series in Optical Sciences, Vol. 197, *Springer*, 2015.

[71]. M. Hofstetter, M. Schultze, M. Fieß, B. Dennhardt, A. Guggenmos, J. Gagnon, V. S. Yakovlev, E. Goulielmakis, R. Kienberger, E. M. Gullikson, F. Krausz, U. Kleineberg, Attosecond dispersion control by extreme ultraviolet multilayer mirrors, *Optics Express*, Vol. 19, 2011, pp. 1767-1776.

[72]. Y. Ménesguen, S. de Rossi, E. Meltchakov, F. Delmotte, Aperiodic multilayer mirrors for efficient broadband reflection in the extreme ultraviolet, *Applied Physics A*, Vol. 98, 2010, pp. 305-309.

[73]. E. M. Gullikson, J. H. Underwood, P. Batson, V. Nikitin, A soft x-ray/EUV reflectometer based on a laser produced plasma source, *Journal of X-Ray Science and Technology*, Vol. 3, 1992, pp. 283-299.

[74]. R. Kienberger, E. Goulielmakis, M. Uiberacker, A. Baltuska, V. Yakovlev, F. Bammer, A. Scrinzi, T. Westerwalbesloh, U. Kleineberg, U. Heinzmann, M. Drescher, F. Krausz, Atomic transient recorder, *Nature*, Vol. 427, 2004, pp. 817-821.

[75]. M. Kitzler, N. Milosevic, A. Scrinzi, F. Krausz, T. Brabec, Quantum theory of attosecond XUV pulse measurement by laser dressed photoionization, *Physical Review Letters*, Vol. 88, 2002, 173904.

[76]. R. Trebino, K. W. DeLong, D. N. Fittinghoff, J. N. Sweetser, M. A. Krumbügel, B. A. Richman, D. J. Kane, Measuring ultrashort laser pulses in the time-frequency domain

using frequency-resolved optical gating, *Review of Scientific Instruments*, Vol. 68, 1997, pp. 3277-3295.

[77]. Y. Mairesse, A. de Bohan, L. J. Frasinski, H. Merdji, L. C. Dinu, P. Monchicourt, P. Breger, M. Kovačev, R. Taïeb, B. Carré, H. G. Muller, P. Agostini, P. Salières, Attosecond synchronization of high-harmonic soft x-rays, *Science*, Vol. 302, 2003, pp. 1540-1543.

[78]. J. Gagnon, E. Goulielmakis, V. S. Yakovlev, The accurate FROG characterization of attosecond pulses from streaking measurements, *Applied Physics B*, Vol. 92, 2008, pp. 25-32.

[79]. A. Guggenmos, M. Jobst, M. Ossiander, S. Radünz, J. Riemensberger, M. Schäffer, A. Akil, C. Jakubeit, P. Böhm, S. Noever, B. Nickel, R. Kienberger, U. Kleineberg, Chromium/scandium multilayer mirrors for isolated attosecond pulses at 145 eV, *Optics Letters*, Vol. 40, 2015, pp. 2846-2849.

[80]. A. Guggenmos, R. Rauhut, M. Hofstetter, S. Hertrich, B. Nickel, J. Schmidt, E. M. Gullikson, M. Seibald, W. Schnick, U. Kleineberg, Aperiodic CrSc multilayer mirrors for attosecond water window pulses, *Optics Express*, Vol. 21, 2013, pp. 21728-21740.

[81]. C. Montcalm, B. T. Sullivan, S. Duguay, M. Ranger, W. Steffens, H. Pépin, M. Chaker, In situ reflectance measurements of soft-x-ray/extreme-ultraviolet Mo/Y multilayer mirrors, *Optics Letters*, Vol. 20, 1995, pp. 1450-1452.

[82]. R. Soufli, E. Spiller, D. L. Windt, J. C. Robinson, E. M. Gullikson, L. Rodriguez-de Marcos, M. Fernandez-Perea, S. L. Baker, A. L. Aquila, F. J. Dollar, J. A. Méndez, J. I. Larruquert, L. Golub, P. Boerner, In-band and out-of-band reflectance calibrations of the EUV multilayer mirrors of the atmospheric imaging assembly instrument aboard the Solar Dynamics Observatory, *Space Telescopes and Instrumentation 2012: Ultraviolet to Gamma Ray Proceedings of SPIE*, Vol. 8443, 2012, 84433C.

[83]. S. Bajt, Molybdenum-ruthenium/beryllium multilayer coatings, *Journal of Vacuum Science & Technology A*, Vol. 18, 2000, pp. 557-559.

[84]. B. Sae-Lao, C. Montcalm, Molybdenum-strontium multilayer mirrors for the 8-12-nm extreme-ultraviolet wavelength region, *Optics Letters*, Vol. 26, 2001, pp. 468-470.

[85]. C. Montcalm, P. A. Kearney, J. M. Slaughter, B. T. Sullivan, M. Chaker, H. Pépin, C. M. Falco, Survey of Ti-, B-, and Y-based soft x-ray-extreme ultraviolet multilayer mirrors for the 2- to 12-nm wavelength region, *Applied Optics*, Vol. 35, 1996, pp. 5134-5147.

[86]. J. Gagnon, V. S. Yakovlev, The robustness of attosecond streaking measurements, *Optics Express*, Vol. 17, 2009, pp. 17678-17693.

[87]. S. Neppl, R. Ernstorfer, E. M. Bothschafter, A. L. Cavalieri, D. Menzel, J. V. Barth, F. Krausz, R. Kienberger, P. Feulner, Attosecond time-resolved photoemission from core and valence states of magnesium, *Physical Review Letters*, Vol. 109, 2012, 087401.

[88]. A. Aquila, F. Salmassi, E. Gullikson, Metrologies for the phase characterization of attosecond extreme ultraviolet optics, *Optics Letters*, Vol. 33, 2008, pp. 455-457.

[89]. C. Bourassin-Bouchet, S. de Rossi, J. Wang, E. Meltchakov, A. Giglia, N. Mahne, S. Nannarone, F. Delmotte, Shaping of single-cycle sub-50-attosecond pulses with multilayer mirrors, *New Journal of Physics*, Vol. 14, 2012, 023040.

[90]. H. G. Muller, Reconstruction of attosecond harmonic beating by interference of two-photon transitions, *Applied Physics B*, Vol. 74, 2002, pp. 17-21.

[91]. Y. Mairesse, F. Quéré, Frequency-resolved optical gating for complete reconstruction of attosecond bursts, *Physical Review A*, Vol. 71, 2005, 011401.

[92]. X. Wang, M. Chini, Y. Cheng, Y. Wu, X.-M. Tong, Z. Chang, Subcycle laser control and quantum interferences in attosecond photoabsorption of neon, *Physical Review A*, Vol. 87, 2013, 063413.

[93]. M. Schultze, E. Bothschafter, A. Sommer, S. Holzner, W. Schweinberger, M. Fieß, M. Hofstetter, R. Kienberger, V. Apalkov, V. Yakovlev, M. I. Stockman, F. Krausz, Controlling dielectrics with the electric field of light, *Nature*, Vol. 493, 2013, pp. 75-78.

[94]. E. Tea, H. Hamzeh, F. Aniel, Hot carriers relaxation in highly excited polar semiconductors: Hot phonons versus phonon–plasmon coupling, *Journal of Applied Physics*, Vol. 110, 2011, 113108.

[95]. K. Zhao, Q. Zhang, M. Chini, Y. Wu, X. Wang, Z. Chang, Tailoring a 67 attosecond pulse through advantageous phase-mismatch, *Optics Letters*, Vol. 37, 2012, pp. 3891-3893.

[96]. T. Popmintchev, M.-C. Chen, D. Popmintchev, P. Arpin, S. Brown, S. Ališauskas, G. Andriukaitis, T. Balciunas, O. D. Mücke, A. Pugzlys, A. Baltuška, B. Shim, S. E. Schrauth, A. Gaeta, C. Hernández-García, L. Plaja, A. Becker, A. Jaron-Becker, M. M. Murnane, H. C. Kapteyn, Bright coherent ultrahigh harmonics in the keV x-ray regime from mid-infrared femtosecond lasers, *Science*, Vol. 336, 2012, pp. 1287-1291.

[97]. P. H. Bucksbaum, The future of attosecond spectroscopy, *Science*, Vol. 317, 2007, pp. 766-769.

[98]. S. Haessler, T. Balčiūnas, G. Fan, L. E. Chipperfield, A. Baltuška, Enhanced multi-colour gating for the generation of high-power isolated attosecond pulses, *Scientific Reports*, Vol. 5, 2015, 10084.

[99]. M. Ossiander, F. Siegrist, V. Shirvanyan, R. Pazourek, A. Sommer, T. Latka, A. Guggenmos, S. Nagele, J. Feist, J. Burgdörfer, R. Kienberger, M. Schultze, Attosecond correlation dynamics, *Nature Physics*, Vol. 13, 2017, pp. 280-285.